Transport Processes in the Tropical Warm Pool Boundary Layer. Part II: Vertical Structure and Variability

A. G. WILLIAMS AND J. M. HACKER

Flinders Institute for Atmospheric and Marine Sciences (FIAMS), Adelaide, Australia

H. KRAUS

Meteorological Institute of the University of Bonn, Bonn, Germany

(Manuscript received 5 February 1996, in final form 17 January 1997)

ABSTRACT

The structure of the intertropical convergence zone ITCZ cloud-topped marine atmospheric boundary layer away from the most intense mesoscale convective systems during the Tropical Ocean Global Atmosphere Coupled Ocean–Atmosphere Response Experiment (TOGA COARE) is investigated. Eight vertical profiles taken by the Australian Cessna research aircraft are analyzed, representing the successive influence of a growing small cluster of precipitating cumulus upon the subcloud layer. On the basis of conclusions from a spectral analysis in Part I of this study, results are partitioned into contributions from three distinct categories: (a) small-scale (<2 km) processes, corresponding to small eddies contained and forced mainly within the subcloud layer and weakly active cumulus motions; (b) cloud-scale (>2 km) processes, corresponding to meso-γ-scale motions associated mainly with the action of precipitating cumulus clouds and larger motions; and (c) extreme processes, corresponding to contributions from events at the tail of the small-scale statistical flux distribution. Such events are associated with downdrafts below precipitating cumulus, updrafts at gustfronts, and the effects of moisture contamination on thermodynamic data, and can act to significantly skew the flux distribution. In the presence of vigorous cumuli, cloud root circulations (including compensating downdrafts) force significant cloud-scale fluxes in the upper subcloud layer. When conditions become highly disturbed, these fluxes dominate and the vast majority of small-scale humidity transport is concentrated into the cloud root regions. Precipitation produces strong downdrafts and outflows of evaporatively cooled air in the lower subcloud layer, markedly increasing temperature and velocity variances. Neither cloud root circulations nor outflows are supported by cloud-scale buoyancy, with the former being fed by pressure and momentum forces while the latter are formed via small-scale (extreme) buoyancy effects. Small-scale (surface forced) processes moisten and slow the subcloud layer as a whole, while cloud processes cause drying and often acceleration due to enhanced cloud–subcloud-layer exchanges. Processes on all scales lead to net warming of the subcloud layer in the present dataset. Although in zero or low precipitation cases the mean structure of the mixed layer may still be represented to some degree by existing simple zero-order jump models, significant adjustments are required to such models in order to account for the effects of cloud-scale processes under disturbed conditions. In particular, the enhancement of cloud–subcloud-layer exchanges by cloud root processes and the effects of increased horizontal wind variances upon surface fluxes requires attention. A new velocity scale is suggested, based on large-scale vertical velocity at cloud base, which may be useful in the formulation of new parameterizations.

1. Introduction

One of the goals of TOGA COARE (Tropical Ocean Global Atmosphere Coupled Ocean–Atmosphere Response Experiment) was improvement of our understanding of multiscale transport processes in the strongly cloud-affected, low wind-speed atmospheric boundary layer (ABL) of the intertropical convergence zone (ITCZ) (Webster and Lukas 1992). As a step toward this goal, Williams et al. (1996, hereafter referred to as WKH) presented a spectral analysis of data from flights by the Flinders Institute for Atmospheric and Marine Sciences (FIAMS) Cessna research aircraft during TOGA COARE. These flights were conducted in the vicinity of ITCZ cloud clusters but away from the most intense mesoscale convective systems (MCSs). The principal differences between the ITCZ subcloud layer (SCL) and other convective marine SCLs were found in WKH to be due to significant disturbance by 10–50-km-scale motions associated with precipitating cumulus and isolated cumulonimbus clouds, and also strong mesoscale (>50 km) heterogeneity resulting from the action of MCSs (inflows and wakes). These two processes are closely interrelated, since convergences produced by

Corresponding author address: Dr. Alastair G. Williams, Flinders Inst. for Atmospheric and Marine Sciences, School of Earth Sciences, Flinders University, GPO Box 2100, Adelaide 5001, Australia.
E-mail: moagw@es.flinders.edu.au

MCS-scale activity frequently initiate new convection. In fact, it has been suggested that mesoscale convergence in the SCL may be a necessary condition for sustaining bands of precipitating cumulus (Simpson and van Helvoirt 1980). At smaller scales, individual precipitating cumulus clouds can strongly perturb the SCL by drawing up air into updrafts (cloud ''roots'') through associated local pressure perturbations (Emmitt 1978; Yau 1979; Rotunno and Klemp 1982; LeMone et al. 1987; LeMone et al. 1988), as well as enhancing entrainment into the SCL. When significant rain develops, clouds produce strong downdrafts and outflows of evaporatively cooled air in the SCL can initiate new lines of cumulus at their associated gust fronts. The cascade of convective processes from larger to smaller scales results in a lognormal distribution of clouds within ITCZ convection systems (Lopez 1973, 1976, 1977; Houze and Cheng 1977) and, in the SCL, leads to both heterogeneity in the small-scale fluxes and significant direct meso-γ-scale (10–50 km) fluxes (WKH).

Progress in understanding of the influence of multiscale cloud processes upon ITCZ ABL structure has been accelerated in recent years by results from major field programs such as GATE [Global Atmospheric Research Program (GARP) Atlantic Tropical Experiment] and from numerical simulations. Of particular interest has been the emergence of cumulus ensemble models (CEMs) (e.g., Soong and Tao 1980; Krueger 1985, 1988; Lipps and Hemler 1986; Gregory and Miller 1989), which attempt to fill the gap between small-scale ($<$1–2 km) processes and the grid spacings of large-scale models. The influence of mesoscale convective organization upon the interaction between deep cumulus cloud ensembles and large-scale processes, for example, has recently been studied by Xu et al. (1992) using CEM simulations. The simulations of precipitating ITCZ cloud ensembles by Krueger (1985, 1988) are of particular interest, for they have concentrated on the influences of cloud processes upon the subcloud layer and have verified many aspects of SCL structure inferred indirectly from GATE budget, diagnostic, and observational studies. There remains, however, a need for direct verification against in situ aircraft turbulence data. The extent to which cloud-scale and small-scale motions are separable also remains unclear. Results from WKH suggest that small-scale ($<$2 km) processes have an ability to adjust quickly to large-scale variability and, away from sharp changes associated with events such as convective downdrafts and gust fronts, remain well-organized and in quasi equilibrium with local conditions. Sun et al. (1996) have also recently reported evidence of local equilibrium at small scales in the TOGA COARE SCL in their study of the scale dependance of air–sea fluxes using low level ($<$40 m) data from the Electra aircraft.

The current study analyzes a series of vertical profiles (''stacks'' of straight and level flight segments) obtained during Cessna missions in the ITCZ boundary layer during TOGA COARE. These profiles reveal the structure of the ABL in a variety of states, from relatively undisturbed conditions in the late stages of adjustment after the passage of a convective line disturbance to highly disturbed conditions at the edge of a mature MCS, and include examples of well-developed ''warm convection'' (convection with warm rain processes). Since studies of the GATE boundary layer have emphasized the importance of distinguishing between different sizes and stages in the evolution of convective disturbances (e.g., Brümmer 1979; Barnes and Garstang 1982), variations among the individual profiles are highlighted in our study. In addition, results are separated into contributions from high- and low-frequency parts of the spectrum at the crossover wavelength of 2 km suggested by WKH. In the current study, we distinguish between three categories of processes based on this separation: (a) small-scale ($<$2 km) processes, corresponding to eddies contained and forced mainly within the SCL, including surface layer plumes, mixed layer thermals, passive and weakly active cumulus motions [''active'' refers to nonprecipitating cumuli that have reached their level of free convection and are vertically extended, as in the definition of Stull (1985)]; (b) cloud-scale ($>$2 km) processes, corresponding to meso-γ-scale motions associated mainly with the action of strongly active and precipitating cumulus and larger motions (note that cloud scale need not always imply clouds); and (c) extreme events, corresponding to contributions from events at the tail of the small-scale statistical flux distribution. (It will be seen that such events are associated with gust fronts and convective downdrafts, and act to skew the flux distribution.) Attention is also given to effects of moisture contamination on thermodynamic data.

2. The aircraft data

a. The profiles

The data used in this study come from eight vertical profile patterns flown by the Cessna aircraft during TOGA COARE, each comprising several straight and level flight segments, or ''runs,'' at different heights. The runs vary in length from 28 to 122 km overall and cover altitudes from very near the surface to heights varying between 373 and 1075 m for different profiles. All patterns were flown within the TOGA COARE intensive flux array (IFA) region [centered on the IMET buoy at 1°45′S 156°00′E; see Webster and Lukas (1992)]. Meteorological conditions during the flights (based on analyses of flight videos and aircraft data plots) are discussed below and summarized in Table 1. Large-scale 1000-hPa European Centre for Medium Range Weather Forecasts (ECMWF) streamline plots for the TOGA COARE area were obtained from Asencio et al. (1993) and corresponding divergence plots were obtained courtesy of J. Redelsperger (Meteo France).

TABLE 1. FIAMS' Cessna data used in this study.

Flight ID/ No. runs	Start date	Start time (UTC)	Latitude/Longitude (profile midpoint)	Height range of runs (m)	Length range of runs (km)	Overall conditions	Rank
7/5 runs	19 Jan 1993	00:35	2°03′S 155°09′E	22.2–373.1	50–122	Strengthening deep convection near a mature MCS	8
a/6 runs	26 Jan	23:03	1°53′S 154°55′E	18.7–789.8	58–94	Late stages of adjustment in the wake of a large convection band (undisturbed)	1
b/4 runs	27 Jan	23:04	2°13′S 154°53′E	21.3–890.1	47–54	Well-developed warm convection	6
b/4 runs	28 Jan	00:20	2°28′S 154°29′E	26.6–431.8	28–38	Well-developed warm convection	7
c/8 runs	28 Jan	23:12	1°40′S 155°15′E	20.7–1036.2	32–55	Developing small cloud cluster	5
e/8 runs	3 Feb	23:21	1°42′S 156°09′E	19.8–1075.8	39–56	Active cumulus beneath a complex mesoscale layer cloud deck	2
h/5 runs	13 Feb	23:20	2°45′S 153°05′E	21.3–944.9	53–75	Early growing stage of a small cloud cluster	4
h/5 runs	14 Feb	01:05	2°45′S 153°05′E	21.1–956.6	56–68	Early growing stage of a small cloud cluster	3

For organizational purposes, each profile has been given a rank indicating the strength of ABL cloud activity as perceived in the analyses below, with rank 1 being the weakest. The profiles will subsequently be referred to by their rank.

1) 19 JANUARY 1993: RANK 8

Strengthening deep convection near a mature MCS. This north–south profile was flown 50 km southeast of the edge of a mature MCS. Streamline–divergence plots reveal that the runs were south of a strong east–west line of convergence. Bands of precipitating cumulus and higher level layer cloud were spreading southward and developing. The profile was situated below two such bands of cloud, oriented approximately east–west across the flight track. The flight data exhibit two 30–40-km regions of cool, strongly disturbed air associated with the cloud bands, edged with sharp jumps back to warmer, more homogeneous conditions.

2) 26–27 JANUARY 1993: RANK 1

Late stages of adjustment in the wake of a large convection band (undisturbed). This north–south profile was north of a long (1000-km) band of convection that had passed through the profile position a few hours before and was now moving away to the southwest and decaying. Streamline–divergence plots and aircraft sounding data indicate strong subsidence (divergence) in the region. Conditions were almost undisturbed, with only a slight gradient toward cooler temperatures in the south. Weak variability is evident on 10-km scales, associated with small active ABL cumulus. Bands of high-level layer cloud in the south part of the track do not appear to be affecting the SCL.

3) 27–28 JANUARY 1993 (2 PROFILES): RANKS 6 AND 7, RESPECTIVELY

Well-developed warm convection. These two north–south profiles were located immediately northeast of a long band of small cloud clusters associated with a line of convergence near New Ireland, Papua New Guinea Streamline–divergence plots indicate weak convergence, and the data from both profiles exhibit strong variability on 30-km scales, associated with precipitating cumulus evolving near and/or advecting across the line of the track. Sharp temperature jumps are evident in the data, corresponding to gust fronts. The second profile (southwest of the first) contains a larger number of precipitating cumuli and is more strongly disturbed. Despite the observation of frequent rainshowers, corresponding satellite infrared images exhibit little cloudiness in this region, indicating that cloud tops were not reaching the highest levels.

4) 28–29 JANUARY 1993: RANK 5

Developing small cloud cluster. A region of precipitating cumulus occupied the southern part of this north–south profile, with active but nonprecipitating cumulus in the north. Streamline–divergence plots indicate parallel flow or slight convergence. All runs exhibit significant variability on 10-km scales, with a strong temperature front penetrated in the southern part of the final leg. High-level layer cloud was present throughout the pattern.

5) 3–4 FEBRUARY 1993: RANK 2

Active cumulus beneath a complex mesoscale layer-cloud deck. This east–west profile had its first 2–3 legs beneath the western edge of a 500-km-wide region of layer cloud passing rapidly through the IFA from east to north (perhaps a remnant of earlier convection), below which were active (nonprecipitating) ABL cumulus. Later legs were in a region of open sky and active cumuli to the west and overcast layer cloud to the east. The data exhibits weak variability on 10-km scales, probably associated with the active ABL cumulus. Streamline–

TABLE 2. Surface fluxes, mixed layer mean values (''ML''), and scaling parameters.

Rank	h (m)	q_{ML} (g kg^{-1})	θ_{ML} (°C)	θ_{eML} (°C)	ML Wind Speed (m s^{-1})	ML Wind Dir (°)	[a]Turning above ML (°/km)	[b]Div ($\times 10^{-5}$ s^{-1})	[c]SST (°C)	E_0 (W m^{-2})	H_0 (W m^{-2})	H_{v0} (W m^{-2})	u_{*0} (m s^{-1})	w_* (m s^{-1})	q_* (g kg^{-1})	θ_* (°C)	t_* (min)
1	660	17.5	27.7	72.2	4.5	149	??	1.0	30.0	65.8	4.6	9.5	0.1428	0.540	0.0404	0.0137	20.4
2	650	17.1	27.5	70.9	4.2	324	−50	0.5	29.8	65.2	2.4	7.3	0.1259	0.493	0.0403	0.0116	22.0
3	[d]470	18.8	27.6	75.3	6.7	285	−50	0.0	29.2	123.0	1.5	10.7	0.2094	0.502	0.0745	0.0166	15.6
4	[d]440	18.9	27.3	75.0	6.3	284	−50	0.0	29.0	113.6	1.0	9.5	0.1898	0.464	0.0761	0.0152	15.8
5	520	18.2	27.8	74.1	5.9	273	??	−0.5	30.0	76.5	2.1	7.8	0.1765	0.463	0.0531	0.0128	18.7
6	440	17.9	27.8	73.3	7.2	323	−30	−0.5	30.1	81.2	2.2	8.3	0.1744	0.440	0.0566	0.0136	16.7
7	[d]400	18.7	27.1	74.4	7.4	299	−30	−1.0	30.0	110.6	4.5	12.8	0.2030	0.501	0.0674	0.0194	13.3
8	[d]400	18.5	27.5	74.4	8.1	297	−200	−2.0	30.0	132.4	12.3	22.4	0.2694	0.587	0.0758	0.0268	11.3

[a] Approximate wind turning rate with height above mixed layer, positive clockwise.
[b] Approximate large-scale ECMWF 1000-hPa divergence (J. Redelsperger 1996, personal communication).
[c] Radiometric sea surface temperature from lowest run in profile.
[d] LCL used to define h. Note: mixed layer height for profiles 7 and 8 is revised to 0.6h (240 m) during the analysis in Chapter 5.

divergence plots indicate parallel or slightly divergent (subsident) flow.

6) 13–14 FEBRUARY 1993 (2 PROFILES): RANKS 4 AND 3, RESPECTIVELY

Early growing stage of a small cloud cluster. These southwest–northeast profiles were immediately west of a small developing cloud cluster. Small bands (10–20 km across) of high-level layer cloud advected over the transect during the patterns. The northeast end of the first profile was quite close to the developing cloud cluster, which moved farther away during the second profile. A line of active (nonprecipitating) cumulus was developing across the middle of the transect during the first profile, indicating minor convergence, although large-scale streamline–divergence plots indicate parallel flow. In the second profile, a few small cumuli were developing in the southern part. The data exhibit moderate variability on 10–20-km scales, associated with the buildup to the northeast as well as the action of local active cumulus.

7) LOCATION OF DATASET WITHIN THE SPECTRUM OF ITCZ CONVECTIVE PROCESSES

The eight vertical profiles described above span an interesting subrange of ITCZ boundary layer types. The four lowest ranked profiles (1–4; see Table 1) contain progressively numerous and stronger active (nonprecipitating) cumulus clouds, while profiles 5–8 contain precipitating cumulus. Profile 5 contains a few raining clouds, while profiles 6 and (especially) 7 represent well-developed warm convection. Finally, profile 8 represents the most severe convection conditions FIAMS' small Cessna could safely endure in the vicinity of an MCS. In terms of the cycle of major convective disturbances investigated in budget studies such as those of Brümmer (1979) and Thompson et al. (1979) during GATE, our cases span only the categories of ''undisturbed'' to ''growing'' (and perhaps the late stages of decay). Yet it is clear that the ABL sampled by the FIAMS aircraft is considerably more disturbed than the GATE fairweather ABL investigated by Nicholls and LeMone (1980) and others. With the possible exception of profile 8, this dataset can be regarded as representing the progressive influence of a growing small cluster of precipitating cumulus on processes in the marine ABL. Profile 8 represents a link between such systems and the more intense MCSs.

b. ABL parameters and large-scale context

Selection of a suitable scaling height (h) for this study proved difficult, as the subcloud layer was rarely found to be well mixed and its height is expected to vary considerably in response to mesoscale changes. Many aircraft soundings were extremely hard to interpret for this reason; also because they were often constructed piecewise from climbs between individual runs (and thus reflected horizontal changes existing in mean levels from one end of a pattern to the other). Estimates of lifting condensation level (LCL) were often different from cloud-base observations by pilots and observers, and, in any case, LCL has sometimes been found by others to fall above the top of the subcloud mixed layer (e.g., LeMone 1980b). It was eventually decided to use mixed layer height for h where possible, defined as the height at or below LCL at which the slopes of the vertical distributions of run-averaged state variables first start to change towards their cloud layer and free atmosphere values. In cases where this height proved to be impossible to define, LCL was used for h (ranks 3, 4, 7, and 8). Table 2 presents h, estimated surface fluxes, mixed layer averaged quantities, and the mixed layer scaling parameters for velocity, temperature, humidity, and time:

$$w_* = \left[\frac{gh}{\overline{\theta_v}}\,\frac{H_{v0}}{\rho c_p}\right]^{1/3}, \qquad \theta_* = \frac{H_0/\rho c_p}{w_*}, \qquad q_* = \frac{E_0/\rho L_w}{w_*},$$

$$t_* = h/w_*,$$

where E, H, and H_v denote fluxes of latent heat, sensible heat, and buoyancy, respectively; θ_v is virtual potential temperature; ρ is air density; g is acceleration due to gravity; c_p is specific heat of moist air.

Surface fluxes (indicated above by a ''0'' subscript) were obtained by extrapolation of average small-scale fluxes (see below) to $z = 0$. Wind turning rate with height above the mixed layer is approximated from available aircraft data, and large-scale divergence is estimated from the ECMWF 1000-hPa divergence analysis charts (J. Redelsperger 1996, personal communication). Mean vertical air velocity was not obtainable from the aircraft data (see section 2c below).

The six flights from 27 January to 14 February (ranks 6, 7, 5, 2, 4, and 3) encountered west-northwest mean winds in the ABL (Table 2), reflecting the prevailing synoptic conditions during the third prominent westerly wind episode in the IFA region during TOGA COARE [late January to end of February; see Lin and Johnson (1996)]. The first two flights (19 and 26 January: ranks 8 and 1) were set in large-scale easterly flow prior to the westerly wind episode, although the 19 January (rank 8) profile exhibits northwest winds due to the influence of the nearby MCS [see section 2a(1)]. The aircraft data generally showed a strengthening and counterclockwise turning of the wind vector with height above the LCL (Table 2), also in agreement with the overall large-scale picture during westerly wind episodes.

Large-scale vertical velocities (as indicated by the 1000-hPa divergence estimates in Table 2) were directly correlated with rank. It is well known that in the Tropics convection is associated with mean rising motion. Mean SCL wind speeds also showed a general increase with rank. Although increased surface evaporation resulting from higher SCL wind speeds may act to promote convection, it is also possible that enhanced entrainment of high-momentum air from above the SCL in the presence of increasing clouds and rain can increase mixed-layer wind speeds. Such feedbacks between surface fluxes and convection have been offered as explanations for certain large-scale convection cycles including the 30–60-day oscillation (Emanuel 1987; Neelin et al. 1987), and although the results of Lin and Johnson (1996) do not support this as a significant overall forcing mechanism for large-scale convection during TOGA COARE, its importance on local scales cannot been precluded.

Surface latent heat fluxes (in the range 65–132 W m^{-2}) were well correlated with wind speed (and therefore rank), while surface sensible heat fluxes were not, being generally very small (a few W m^{-2}) except in the highest ranked deep convection case (12 W m^{-2}). This is again in agreement with Lin and Johnson (1996), who report a (negative) correlation of sensible heat flux with GMS brightness temperature, linking H_0 with gustiness and cool downdrafts underneath deep convection. Values of h varied between 400 and 700 m with a general trend towards lower values with increasing rank, in agreement with the results of others that the mixed layer depth is typically lowered in disturbed conditions (Mandics and Hall 1976; Zipser l977; Echternacht and Garstang 1976). It should be remembered that LCL was used to define h for ranks 3, 4, 7, and 8 (Table 2).

c. Special data issues

See WKH for a more detailed discussion of these issues. The low-frequency part of the vertical aircraft velocity component, which is usually calculated using differentiated altitude computed from static pressure, was found from radar altimeter data for these flights over the ocean. This removes possible spurious effects of horizontal pressure variations upon the computed vertical wind component (w) within runs, but estimates of large-scale mean vertical velocities are still not possible, since typical magnitudes of the run-mean w are below the accuracy of the aircraft's instrumentation. Estimates of mean w are obtainable from aircraft data only via special flight patterns designed to measure horizontal convergences at several heights (Gultepe et al. 1990).

Since rain was sometimes encountered during the flights, contamination of temperature and humidity data by liquid water effects is a possibility (Lenschow and Pennell 1974; LeMone 1980a). Below cloud base, rain was mainly encountered in sharp downdrafts below precipitating cumulus clouds and lines of convective activity. When flying in the cloud layer, however, contamination is expected to be more common, and careful note will be made of such data in the discussion of results.

3. Analysis techniques

a. Partitioning into small- and cloud-scale motions

Over an entire aircraft run, we can represent any air property of interest by $a = \langle a\rangle + a' + a''$, where $\langle a\rangle$ is the overall run mean; and a' and a'' represent deviations from the mean due to cloud- and small-scale motions, respectively. Small-scale includes all wavelengths up to some cutoff to be determined, and cloud-scale includes wavelengths between that cutoff and the run length. It can easily be shown that the covariance of two quantities, a and b, over an entire run is then given by

$$F_{ab} = \langle ab\rangle - \langle a\rangle\langle b\rangle = C_{ab} + S_{ab} + X_{ab}, \qquad (1)$$

where

$$C_{ab} = \langle a'b' \rangle \quad \text{cloud-scale term}$$

$$S_{ab} = \langle a''b'' \rangle \quad \text{small-scale term}$$

$$X_{ab} = \langle a''b' \rangle + \langle a'b'' \rangle \quad \text{cross terms.}$$

Choosing a simple nonbiased Reynolds averaging technique to define our small-scale motions, we set $a'' = a - \bar{a}$ in any small-scale block of length L, where the overbar operator indicates a simple mean value (i.e., all data points are used and given equal weighting) taken over the block. Applying this technique to equally sized contiguous blocks over the entire run, our cloud-scale motions are then given by $a' = \bar{a} - \langle a \rangle$ and are constant within any given small-scale block. For this type of unbiased averaging, the cross terms $X_{ab} = 0$ (e.g., Sun et al. 1996) and $S_{ab} = \langle \overline{a''b''} \rangle$, the ensemble mean of all the local small-scale block covariances in the aircraft run. As will be seen later, a simple mean may prove to be an undesirable estimator for the ensemble expected value of the local small-scale block covariances, S^*_{ab}. We therefore introduce the term S^{**}_{ab}, such that $S_{ab} = S^*_{ab} + S^{**}_{ab}$, and Eq. (1) becomes

$$F_{ab} = C_{ab} + S^*_{ab} + S^{**}_{ab}. \tag{2}$$

It remains to choose a value for the block length defining small-scale motions. From the results of WKH, the 2-km wavelength marks a transition between two different spectral regimes, with smaller scales corresponding to eddies contained (and forced) mainly within the ABL and weakly active cumulus motions, while larger scales correspond to active and precipitating cumulus, small cloud clusters, and so on. Since none of the cospectra in WKH exhibit a spectral gap near 2 km, we cannot hope for even local insensitivity of the flux obtained to cutoff wavelength in TOGA COARE data. Instead, we must rely upon the interpretation that the spectrum of small-scale processes extends to wavelengths no greater than 2 km, while that of cloud-related processes impinges upon the small scales due to the effects of cumulus roots and extreme events (gust fronts and convective downdrafts). With this interpretation, we choose the shortest possible cutoff wavelength, in order to minimize the effects of spectral intrusion from larger-scale motions, and set $L = 2$ km.

The following abbreviations for the small-scale fluxes in energy units will be used from time to time in the remainder of the paper:

Latent heat: $E = \bar{\rho} L_w \overline{q''w''}$ (W m^{-2})

Sensible heat: $H = \bar{\rho} c_p \overline{\theta''w''}$ (W m^{-2})

Alongwind momentum: $\tau_x = \bar{\rho} \overline{u''w''}$ (N m^{-2})

Across-wind momentum: $\tau_y = \bar{\rho} \overline{v''w''}$ (N m^{-2})

where the along- (x) and across- (y) wind directions are defined relative to the run-averaged wind vector.

b. Expected sources of uncertainty

Whereas small-scale statistics are expected to contain little bias due to undersampling of the contributing wavelengths (most small-scale eddies are resolved in wavelengths <2 km), this is not true of cloud-scale statistics. Contributions to these are seen on scales up to and beyond 50 km in WKH, and we therefore expect a bias due to undersampling of contributing wavelengths. Similarly, the population of small-scale eddies is very well sampled in these generally quite long runs, while that of cloud-scale eddies is undersampled.

As discussed above, certain features of the cloud-scale eddies are not restricted to wavelengths longer than 2 km. In particular, the spectral signal of extreme features such as gust fronts and convective downdrafts may extend well into high wavenumbers. A possibility therefore exists of contamination of small scales by cloud-scale processes. As stated in section 2c, we also expect some liquid moisture contamination of data during extreme events and in-cloud runs. The difficulty of obtaining accurate values for $\langle w \rangle$ over large distances from aircraft data has also been discussed in section 2c.

4. Characteristics of the partitioned data

a. An example from the data

Figure 1 presents time series of q, θ, and w, 2-km blocked small-scale fluxes and contributions to the cloud-scale fluxes ($a'w'$), for the 250-km ''ferry run'' preceding the highly disturbed profile ranked 8 (also used as an example in WKH). The small-scale fluxes are computed as simple covariances of a 2-km block, moved along by one sample each time so that the original resolution of the series is maintained. While this is the best method for displaying details in time series plots, we note that in the statistical analyses to come, the blocks used will be *independent* (moved along by 2 km each time), as implied in section 3.

A 100–150-km region of cool, disturbed air in the centre of Fig. 1 probably corresponds to a cold pool with a locally shallow mixed layer. Vigorous cumulus activity was observed in the region, and state variables show strong variations on 20–50-km scales. Strong heterogeneity on cloud scales is apparent not only in the basic variables but also in the fluxes. The 2-km blocked small-scale latent heat flux E, for example, ranges from 0 to 200 W m^{-2} over the run and displays variability on a range of space scales. On the 20–30-km scale in particular, patterns of E fluxes are clearly related to features in the specific humidity series. Small regions of high amplitude, or ''spikes,'' can be seen in the 2-km flux series, usually occurring in the vicinity of sharp changes in the data. These spikes can be of either sign and appear to be particularly strong in the (small scale) sensible heat flux H. Although we recall from section 2c that instrument wetting is chiefly expected during extreme events, rain contamination can nevertheless be

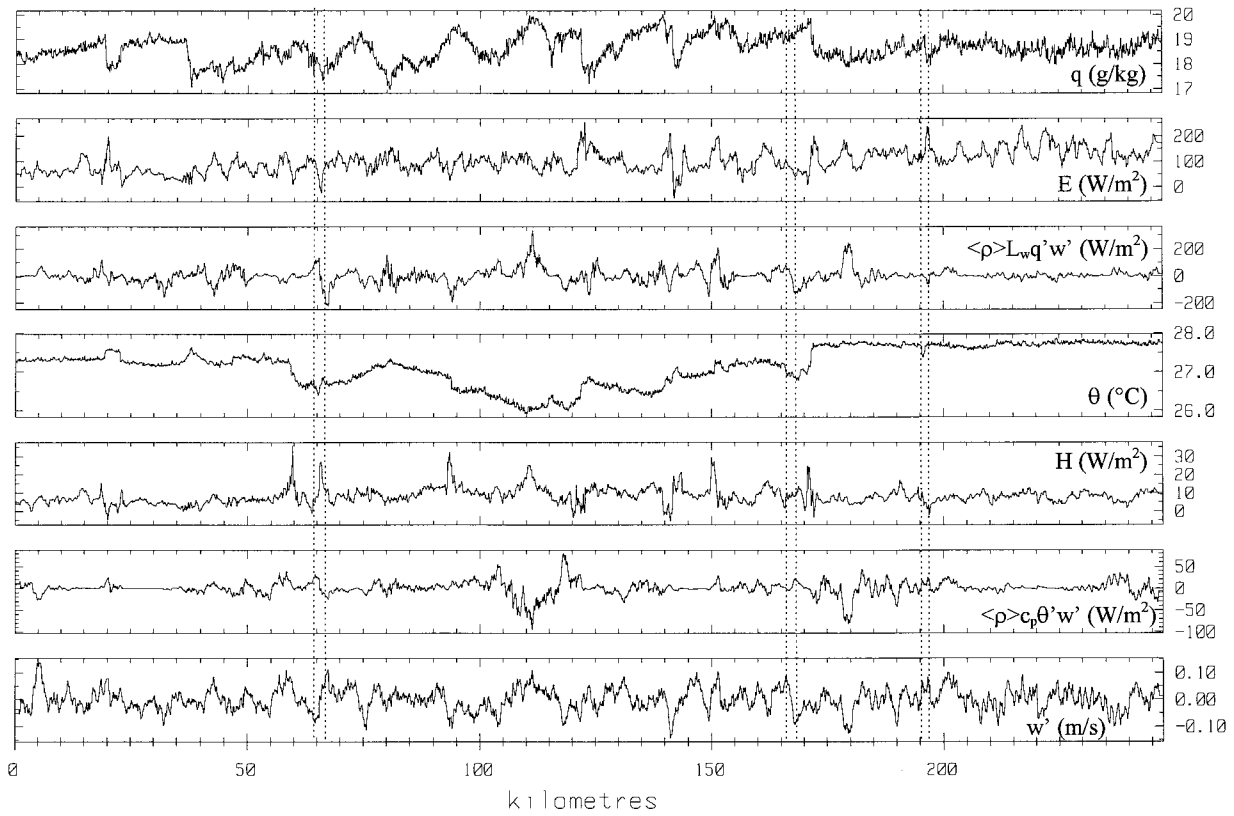

FIG. 1. Example time series of specific humidity (q) and potential temperature (θ), together with 2-km running block averages of vertical velocity (w'), small-scale latent (E) and sensible (H) heat fluxes, and contributions to the corresponding cloud-scale fluxes, from ferry flight 7.1fa, 18 January 1993. Mean altitude: 37.2 m. Rain events seen on aircraft video are marked with vertical lines.

precluded as the major source for these features, since rain events recorded on the flight videos (overlooking the temperature–humidity sensors on the aircraft nose) are relatively rare, and it is clear that many of the spikes do not correspond to times when the aircraft directly encountered rain (see Fig. 1). The occurence of these spikes in the flux series therefore indicates that strong local vertical transport is present. This is a matter that requires attention if the effects of downdrafts and gust fronts upon small-scale fluxes are to be understood. In the case of a gust front, vertical transport is expected to be generated by organized cross-frontal circulation dynamics (Charba 1974; Goff 1976).

Block-averaged w' can locally be as high as 0.1 m s^{-1}, producing significant individual $a'w'$ values. In the case of latent heat, these range by 400 W m^{-2}, and although the ensemble means (corresponding to the cloud-scale fluxes) are quite small in this near-surface case, we can nevertheless see a potential for significant cloud-scale fluxes.

b. Frequency distribution of the small-scale fluxes

Combined normalized frequency distributions of the ensemble of small-scale latent (E) and sensible (H) heat flux values, grouped into height categories, are shown in Figs. 2a and 2b. On each histogram is included the Gaussian distribution for comparison. The combined distributions are generally found to be single peaked, with a positive kurtosis (higher peak and lower extremes compared with the Gaussian distribution) and a slight positive skewness (peak to the left of the mean value). Most flux values in the combined distributions fall within two standard deviations of the mean, with only a few outlying extreme values. The positive kurtosis increases with height and, in group 4 (corresponding to altitudes at and above cloud base), most fluxes fall within only one standard deviation of the mean.

The only slight skew in the combined histograms of H appears to be in contradiction to the case example given in Fig. 1 and is a rather misleading result. In reality, individual histograms of H and E can be quite strongly skewed and the sign of this skew can be either positive or negative, with small positive values being produced only on average. Skewness values for individual runs range between -4 and $+4$, including many close to zero. As an example, Fig. 2c shows the individual histograms for E in group 4, including the four in-cloud runs. The histograms become skewed when the majority of the strong and relatively infrequent extreme events happen to have the same sign.

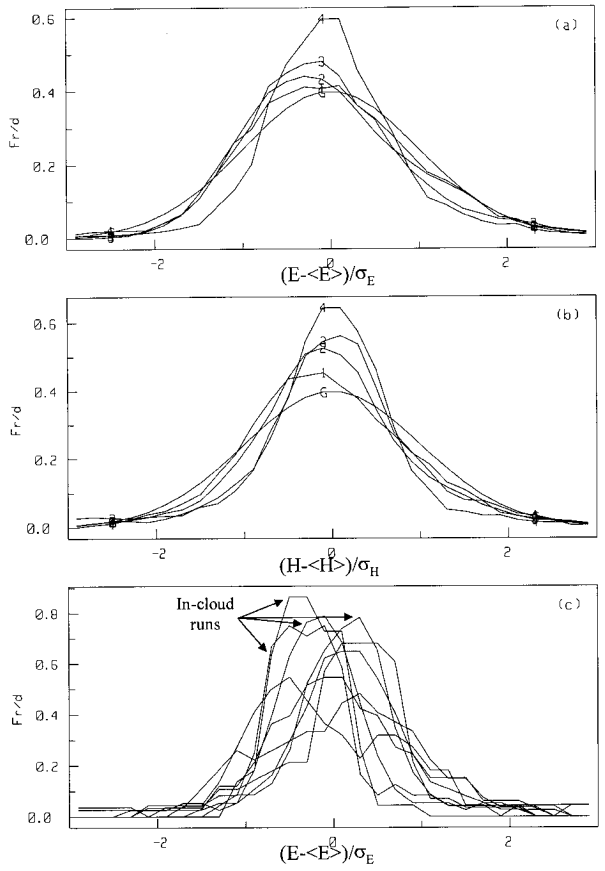

FIG. 2. Frequency histograms of the ensemble of 2-km blocked small-scale fluxes of (a) latent and (b) sensible heat, normalized and averaged into the following height categories: 1) 0–30 m, 2) 50–125 m, 3) 150–430 m, and 4) 580–1100 m; lines marked with a ''G'' are Gaussian distributions (for comparison). (c) Individual latent heat histograms for group 4: in-cloud runs are indicated. Ordinates of all graphs are Fr/*d*, where Fr is the fraction of 2-km blocks in a run falling into each amplitude interval on the abscissa, and $d = 0.2$ is the width of each interval.

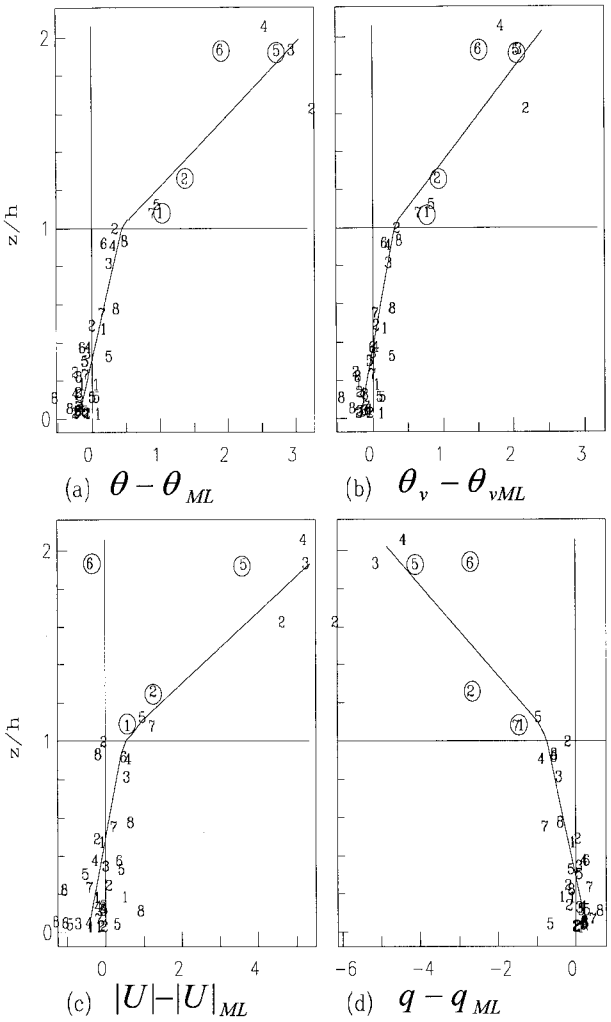

FIG. 3. Vertical distribution of run-average quantities, with the SCL-mean values for each profile removed: (a) potential temperature, (b) virtual potential temperature, (c) wind speed, and (d) specific humidity. Numbers identify the profile rank (see Table 1). In-cloud data are marked with circles.

c. A new expected value for small-scale covariances

The evidence presented above indicates that a simple mean is an undesirable estimator for the ensemble expected value of the local small-scale block covariances, S^*_{ab}, identified with the peak value of the frequency histogram. A combination mean–mode approach for estimating S^*_{ab} is therefore used, in which the ensemble of blocked covariances is first sorted into order of ascending magnitude before selecting only the middle 20% of values and computing their mean. This method provides an expected value that is always close to the peak of the frequency distribution. Following this approach, the term S^{**}_{ab} as defined in section 3a reflects the difference between the peak of the flux histogram and the mean value, thus representing the combined effects of all extreme events in a flight leg (because these events act to skew the histogram, making the mean different from the peak value). Since the flux histograms were on average only slightly skewed, it is expected that S^{**}_{ab} will be small on average but individual flight legs exhibiting a high skewness will have a correspondingly high value of S^{**}_{ab}.

5. Boundary layer structure and variability

a. Mean quantities

The vertical distributions of run-averaged quantities are similar for all eight profiles and are presented in combined form (Fig. 3). Curves are hand fitted to the data to help visualize the interpretation given, and the four in-cloud runs are marked with circles. Here, θ, θ_v, and wind speed (Figs. 3a, 3b, and 3c, respectively) all increase with height through the mixed layer, followed by steeper increases above cloud base (θ increases more

steeply than θ_v). Specific humidity (q; Fig. 3d) decreases slowly through the mixed layer and then drops rapidly above. Equivalent potential temperature (θ_e; not shown), which is conserved during evaporation and condensation processes, has a similar form to q, dropping by 1–2 K on average through the mixed layer, and then by a further 8 K or so up to $z = 2h$. Run-averaged wind directions (not shown) show little run-to-run variability (generally of the order of 10°–20°) and no consistent trend with height in the mixed layer. Directly above the mixed layer, winds generally turn slightly counterclockwise with height, as discussed in section 2b.

The weak vertical mixing within the mixed layer implied by these sloping distributions is evidence of strong entrainment and cloud-scale downdrafts into the mixed layer from above, where the air is drier, warmer, and faster moving. These processes are enhanced by velocity shear above the mixed layer top (Fairall 1984) and by the presence of active and precipitating cloud motions. Echternacht and Garstang (1976) found positive lapse rates of θ_v extending throughout the Barbados Oceanographic and Meteorological Experiment (BOMEX) subcloud layer under disturbed conditions, while in undisturbed conditions the lapse rates were neutral or even slightly unstable. They concluded that cloud-scale downdrafts were strongly affecting mixed-layer budgets under disturbed conditions. The GATE fairweather ABL discussed in the aircraft study of Nicholls and LeMone (1980) was considerably better mixed than that of our study, with mean quantities fairly constant below cloud base. Of the four days analyzed in that study, day 243 represented the most enhanced convective conditions and mean vertical distributions for that day bear the most similarity to ours.

Of the four runs flown partially in cloud, two showed significantly cooler and moister air with slower wind speeds. Since wetting of temperature and dewpoint sensors (mean humidities are obtained from a dewpoint mirror sensor on the Cessna) is known to result in spuriously low temperatures and high humidities, no conclusions can be made respecting these quantities. The slower wind speeds in cloud, however, are likely to be real.

b. Small-scale variances

Run-averaged small-scale variances (S^*_{aa}) are shown in Fig. 4. To minimize the total number of plots without obscuring the character of individual profiles, the first three pairs of profiles (1–2, 3–4, and 5–6) are displayed together. With the exception of horizontal wind components (see below), all quantities scale well with mixed-layer scaling parameters in the lower half of the SCL but become more scattered above. This is presumably a consequence of variations in the intensity of cloud and entrainment related processes.

The quantities θ, θ_v, q and θ_e (the latter not shown) behave similarly, with maxima close to the ground and near $z = h$, where intrusions of warm dry air are common and local changes in SCL depth affect statistics. Exceptions are profiles 6 and 7, which do not exhibit an upper maximum in q variance, and profile 8, in which all small-scale variances are small near the mixed layer top. In profile 7, the upper maxima in θ and θ_v occur below $z = h$. This has not been seen before and probably reflects an inappropriately high value for h. We recall from section 2b and Table 2 that LCL has been used to estimate h in profiles 3, 4, 7, and 8. In the case of θ and q, variance at h is often several times greater than at the surface, while for θ_v it is of a similar magnitude (in agreement with the slower increase above). Large variances of θ and q at $z = h$ have also been found in the GATE ABL (Nicholls and LeMone 1980; Nicholls et al. 1982) and other convective ABLs exhibiting strong gradients across the interface (eg. Chou et al. 1986; Khalsa and Greenhut 1987). Wyngaard and LeMone (1980) have expressed the maximum as a function of the gradient across $z = h$. No particular ordering of the magnitude of the $z = h$ maximum with rank is apparent. Variances are particularly large in in-cloud runs, again at least partially due to contamination effects.

Vertical velocity variances (Fig. 4) show a consistent maximum of approximately 0.5 at $z/h = 0.3$–0.4, with little variation among the individual profiles. A similar form has been seen in other studies under a range of conditions (e.g., Young 1988; Nicholls and LeMone 1980), and the present results confirm that small-scale w variance is little affected by the presence of clouds. Both horizontal velocity components (u:along-, v: across-wind) exhibit high variance close to the surface, decreasing with height. Such behavior has usually been attributed to shear generation in other studies (e.g., Chou et al. 1986; Pennell and LeMone 1974). As pointed out in the trade wind study of Pennell and LeMone (1974), however, such forcing mainly affects the along wind (u) component. In contrast, our results are symmetric in u and v, perhaps reflecting a symmetric production of small-scale horizontal variance by density current outflows below precipitating cumulus, or in the lower ranked situations, merely the light winds. A smaller maximum (or inflection) of u and v variance at $z = h$ is also apparent, perhaps associated with entrainment in the presence of windshear (Fairall 1984). Again, variances appear to be small at $z = h$ in profile 8. Above the SCL, all three small-scale velocity variance components reduce further, with near-zero values being reached around $z = 2h$.

In contrast to the other quantities, the use of mixed-layer scaling does not scale individual u and v variance profiles together well in the lower half of the SCL. These profiles reveal a general shift of variances to greater magnitude with increasing rank. Scaling of these variances with u_* (normally used for neutral boundary layers) and also the convective stress velocity scale (u_*^2/w_*, rather than w_*, fails to improve the plots. In analogy to the convective surface layer situation, in which it is

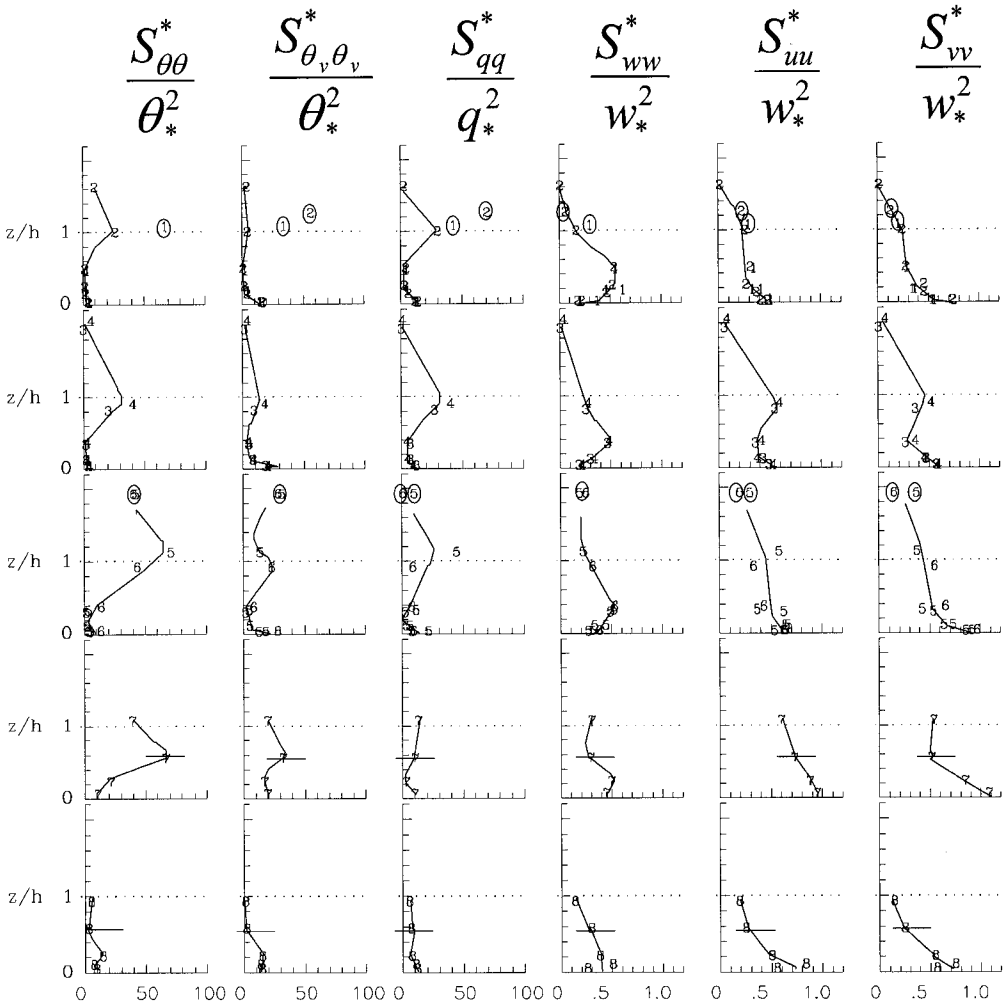

FIG. 4. Vertical distribution of run-average small-scale variances. Rows (top to bottom): ranks 1–2, 3–4, 5–6, 7, and 8; columns (left to right): θ, θ_v, q, w, u, and v. Numbers identify the profile rank (see Table 1). In-cloud data are marked with circles. Short horizontal lines in profiles 7 and 8 indicate revised estimates for mixed layer height, based on the analysis in chapter 5.

well known that the effects of intrusion by mixed-layer eddies produce a scaling of horizontal wind variances with w_* (rather than u_*), the authors expect that mixed layer u and v variances in the TOGA COARE SCL may scale with an external velocity scale. The obvious choices are large-scale vertical motion, which correlates with cloud activity in the present study (see section 2b), and cloud mass flux, which is a direct measure of cumulus activity. The CEM study of Xu and Krueger (1991) has indicated that these two scales are related. This topic is further investigated in section 6d.

c. Cloud-scale variances

Cloud-scale (block-to-block) variabilities of 2-km-mean quantities, C_{aa}, are shown in Fig. 5. Cloud-scale variances of θ, θ_v, q, u, and v are, in general, an order of magnitude greater than their small-scale counterparts, while cloud-scale variances of vertical velocity are 2–3 times smaller, reflecting the effect of proximity to the surface. Profiles 5–8, containing increasingly strong precipitating cumulus, show a strong tendency toward higher cloud-scale variances with increasing rank, in contrast to profiles 1–4 (containing increasingly active but nonprecipitating cumulus), where cloud-scale variances remain relatively low (although still comparable in magnitude to small-scale variances). This establishes beyond doubt a strong link between precipitating cloud activity and disturbance of the SCL at all levels.

The profiles of θ, θ_v, u, and v progress with rank to a state of high variance near the surface, reducing to low values near $z = h$ (scaling of u and v variances will be further investigated in section 6d). For specific humidity and also θ_e (not shown), the situation is reversed, with higher variances appearing at $z = h$. These results agree with the concept of cloud-scale density currents

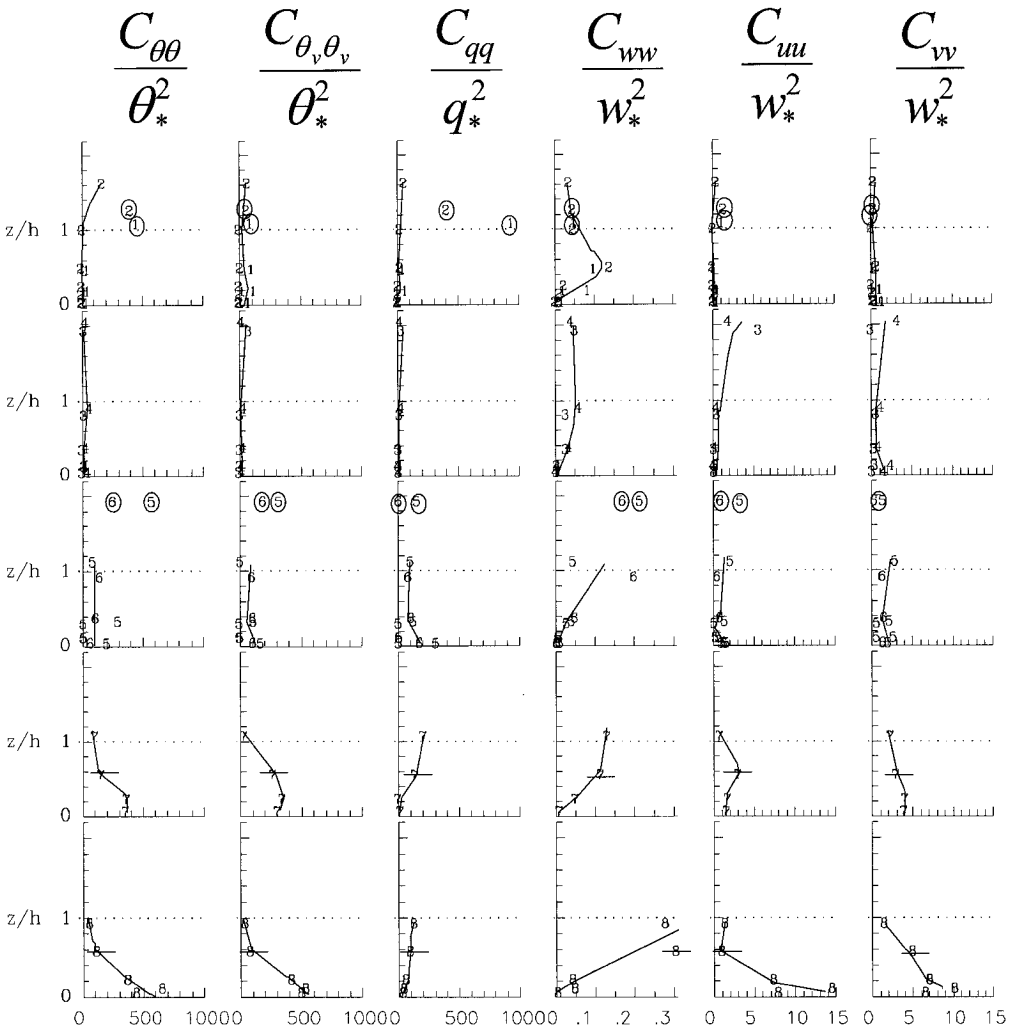

FIG. 5. As for Fig. 4 but cloud-scale variances.

containing evaporatively cooled air from precipitating cumulus clouds, spreading horizontally beneath small-scale (extreme) convective downdrafts. Such air would initially be only slightly more humid than its surroundings, and descent through the negatively sloped mean humidity profile would counteract this difference. The larger cloud-scale q variances near $z = h$ in high ranked stacks is in contrast to the suppressed small-scale variances near $z = h$ (see previous section), perhaps reflecting enhanced organization of moist updrafts into the bases of cumulus clouds (cloud roots) and enhanced entrainment of dry cloud-environment air into cloud-scale downdrafts under disturbed conditions (see later).

Cloud-scale variances of w show a progression towards larger overall values with rank, and while low-ranked profiles (1–4) tend to exhibit a mid-SCL maximum, the high-ranked stacks show generally increasing values with height throughout the SCL. The shapes of our small- and cloud-scale w-variance distributions are in accordance with recent results by Ötles and Young (1996) over land during the Hydrological Atmospheric Pilot Experiment HAPEX. Even their strongly active case (exhibiting increasing cloud-scale w with height) did not involve rain, however, suggesting that our cloud-scale distributions could be a consequence of cloud-root circulations as well as possible density-current processes. With the exception of u and v, in-cloud runs (marked with circles) generally show higher cloud-scale variances.

d. Fluxes

Figure 6a presents small-scale, cloud-scale, and extreme components of the latent heat flux, as defined in section 3a [Eq. (2)]. Small-scale fluxes (S^*_{wq}: first column) decrease with height in all cases except profile 4, with the flux at $z = h$ being 25%–50% of the surface flux and a zero value being reached by $z = 1.5h$ or higher. In profile 4, S^*_{wq} slightly increases with height up to $z = h$, before falling to zero farther above. This

is in agreement with the observation in section 2a(6) that active cumulus was developing across the transect during that profile. In the two highest ranked profiles (7 and 8), the small-scale flux drops much more rapidly with height and is already close to zero by $z = h$.

In all profiles containing precipitating cloud (5–8), the cloud-scale latent heat fluxes are at least comparable in magnitude to the small-scale fluxes, and in the highest-ranked profile (8) they dominate. Cloud-scale fluxes increase with height near the surface, as reported previously in other convective boundary layers (e.g., LeMone 1980b). In the present dataset, maximum values are reached near the top of the mixed layer and generally fall back to near-zero by $z = 1.5h$, with the exception of profile 8, in which the flux remains large above the level of the maximum. In profiles 7 and 8, the maximum appears to be below $z = h$, again indicating that h may be overestimated in these profiles.

Fluxes from extreme events are variable but generally close to zero in profiles 1–7. However, in profile 8 (containing strong fronts), S_{wq}^{**} is significant and similar in shape to the cloud-scale fluxes, supporting the discussion in section 4a that gust fronts can be important contributors to the flux. This is not surprising when it is remembered that in mature MCSs (especially squall lines) such features can dominate the transport. Removal of extreme events into S_{wq}^{**} is particularly effective in the in-cloud runs (marked with circles), and the refined small-scale flux (S_{wq}^{*}) shows greatly reduced scatter. Although high moisture fluxes in the in-cloud runs, predominantly coming from extreme events, fit well with the role of cloud updrafts as moisture transporters, no strong conclusion can be made, due to the unknown effects of moisture contamination in these runs.

Due to the scatter introduced by both the in-cloud data and the varying influence of the cloud-scale flux, the total subrun-scale latent heat flux (F_{wq}) is highly variable and can be increasing or decreasing (Fig. 6a) in the SCL. High variability in flux profiles derived from whole flight runs has also been noted in other studies of cumulus-topped marine ABLs (e.g., Nicholls and LeMone 1980; Nicholls et al. 1982).

The land-based study of Ötles and Young (1996) reported decreasing small-scale (their medium-scale) humidity fluxes with height for all cloud types encountered (from forced to strongly active cumulus), an SCL maximum in the cloud-scale (their large-scale) fluxes in the presence of weakly active cumulus clouds, and an increasing cloud-scale flux up to $z = 0.8h$ for strongly active cumulus. Although this seems to be in good general agreement with our results, we note that their strongest case did not produce rain and the depth of the cloud layer was only around 2 km, reflecting the significantly lower overall humidities over land. Their boundary layer was therefore not disturbed by cloud-scale outflows beneath precipitating cumulus, and their cloud-scale humidity fluxes must have been associated only with cloud root updrafts and compensating environmental downdrafts. The occurence of significant cloud-scale humidity fluxes even in nonprecipitating cases in the current study must likewise be a consequence of cloud root circulations.

The 2D CEM simulations of an ITCZ precipitating cumulus cluster by Krueger (1988) provide perhaps the most direct comparison available to our study. Krueger presents simulations of an undisturbed case, with zero large-scale vertical velocity, and a disturbed case, with a large-scale vertical velocity distribution typical of the most active part of an ITCZ disturbance (near-surface divergences around -2.4×10^{-5} s^{-1}, compared with -2.0×10^{-5} s^{-1} in our profile 8). With a horizontal grid resolution of 1 km (comparable to our small scale) and a horizontal domain size of 30 km (comparable to our individual run lengths), he produces small- and cloud-scale SCL humidity flux distributions for his two cases that match well with ours (see his Figs. 8b and 8d).

The budget analysis of the GATE C-scale triangle by Brümmer (1979) provided composite flux profiles for the ITCZ ABL during stages in the life cycle of convective disturbances. At 3800 km^2, this triangle encompassed horizontal scales of the same order as the length of our aircraft profile runs, so that our ''total'' subrun scale fluxes (F_{wq}) are comparable to his budget-derived fluxes. Brümmer found an increasing latent heat flux with height in the growing and developed stages of convective disturbances (flux divergences being fed by advection at >100-km scales), and decreasing values with height in the undisturbed and decaying stages (flux convergence feeding into the >100-km-scale export). The fact that our total fluxes decrease with height in all profiles except profiles 4 (developing cumulus) and 8 (edge of a large MCS) thus seems to confirm [see section 2a(7)] that our dataset spans the categories of undisturbed to growing disturbances as defined by Brümmer (1979). This is not the whole story, however. Humidity flux profiles are a strong function of the scale and location of observations within the general area, as well as the overall level of disturbance, because cloudiness is locally so variable (e.g., LeMone 1980a; LeMone and Meitin 1984). To illustrate this, we note that budget studies of the fairweather ABL in various parts of the Tropics (Riehl et al. 1951; Augstein et al. 1973; Esbensen 1975) have shown that on the 100–500-km scale, the humidity flux out of the mixed layer top is actually a large fraction (up to 90%) of surface evaporation. The majority of this flux must be concentrated into the small regions of active convection (isolated cumulonimbi) present within such large-scale areas, since the flux out of the top of the ABL in the clearer regions between them is small. Furthermore, LeMone and Pennell (1976) found humidity fluxes greatly enhanced beneath cloud patches on the 5-km scale in a regime for which the humidity flux was decreasing with height on the 30-km scale. Even in the developed stage of a convective disturbance, when the overall flux is diverging, a significant

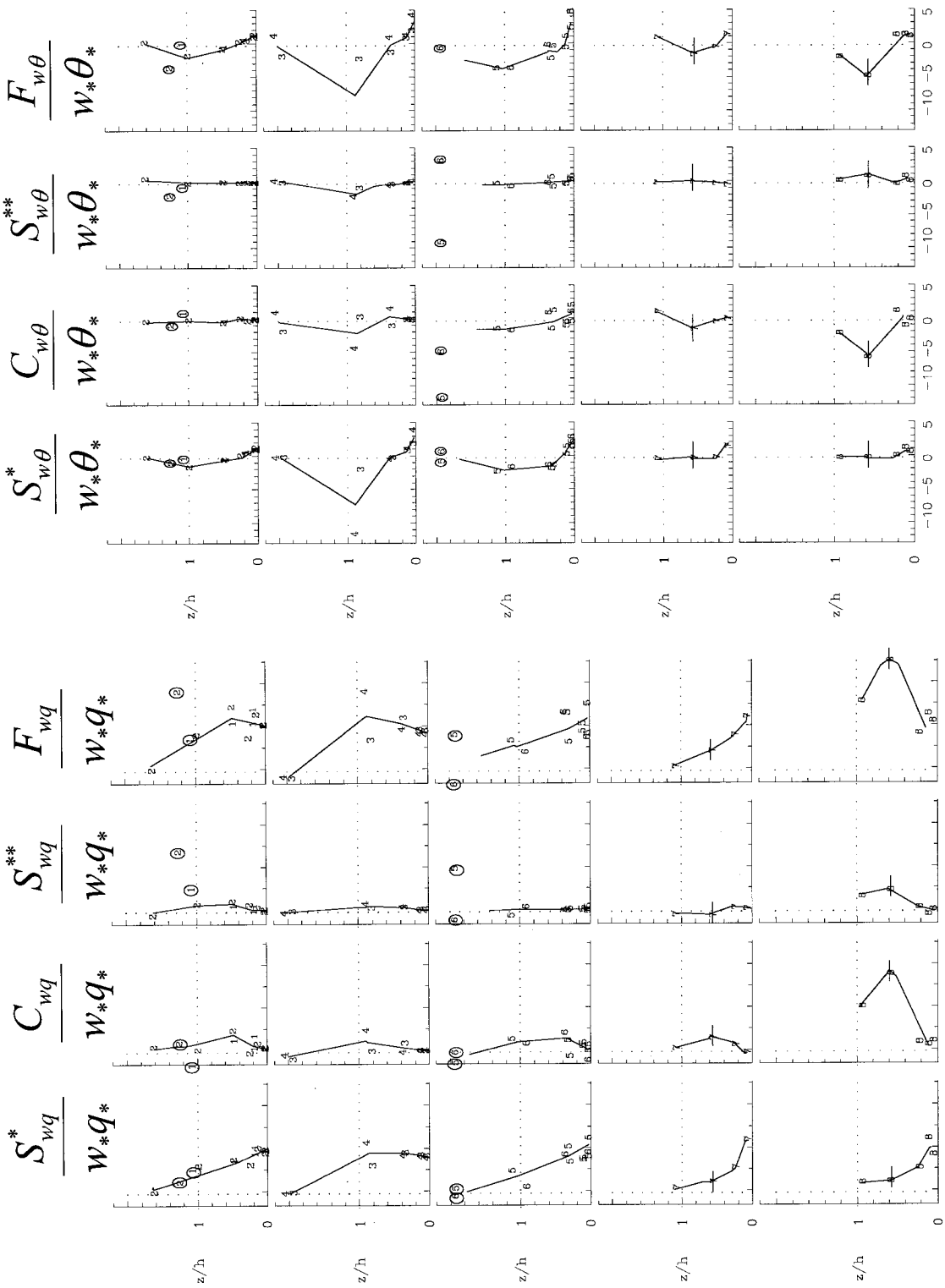

FIG. 6. Vertical distribution of flux terms [see Eq. (2)]. Rows (top to bottom): ranks 1–2, 3–4, 5–6, 7, and 8; columns (left to right): small-scale, cloud-scale, extreme, and total terms. Numbers identify the profile rank (see Table 1). In-cloud data are marked with circles. (a) Latent heat, (b) sensible heat, (c) buoyancy, and (d) alongwind (x) momentum.

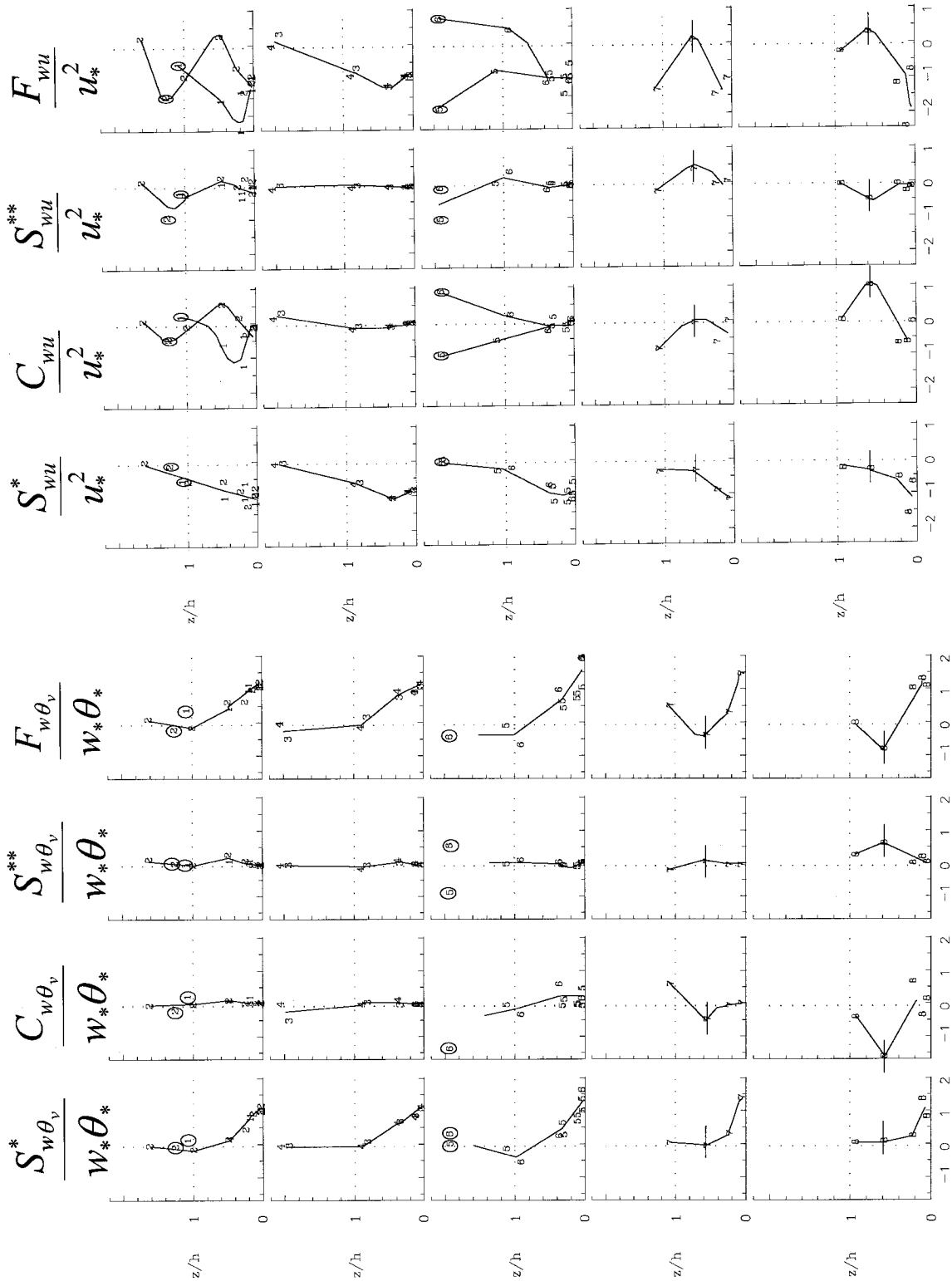

FIG. 6. (*Continued*)

portion of the region will still have little or no cloud cover, due to local subsidence between the large convective towers and, therefore, flux convergence. Thus, our overall flux convergence result may to some extent be an artifact of our tendency to avoid the strongest convection regions in our flights. This observation also applies on the scale of individual runs within our profiles, where results above the SCL are biased by the rarity of in-cloud data and cautious treatment of it when it occurs (due to the possibility of moisture contamination).

The vertical distributions of the small-scale flux of sensible heat (Fig. 6b) are consistent throughout the first six profiles, crossing through zero low down ($z \simeq 0.15h$), remaining negative throughout the remainder of the SCL and reaching zero again at $z = 1.5h$–$2h$. In profiles 7 and 8, the fluxes are close to zero in the upper SCL. Here, $C_{w\theta}$ and $S^{**}_{w\theta}$ are generally small and quite scattered, except in the two highest ranked profiles where $C_{w\theta}$ shows a negative maximum at around $z = 0.6h$ and slight positive values very near the surface. In-cloud anomalies are again well removed from the small-scale fluxes into the extreme term.

Small-scale buoyancy fluxes (Fig. 6c) exhibit the familiar behavior of a decrease to zero values at around $z = 0.6h$, followed by small negative values above. In profiles 1–6, $H_v/H_{v0} \simeq -0.2$ at $z = h$, as in many other studies (e.g., Young 1988). In profiles 7 and 8, upper-SCL small-scale fluxes are again zero or slightly positive, and the cloud-scale flux shows a negative maximum and the extreme flux a positive maximum at $z = 0.6h$. This appears to confirm that the chosen values for h in profiles 7 and 8 are too high, indicating that LCL may significantly overestimate mixed layer height in disturbed conditions. The revised estimates of mixed-layer height for these profiles are 60% smaller (around 240 m in both cases), and are marked in Figs. 4–8.

The CEM results of Krueger (1988) again compare well with ours (see his Figs. 8a and 8c). In contrast, Ötles and Young (1996) reported strong positive SCL maxima in their cloud-scale sensible heat and buoyancy fluxes for strongly active cumulus over land. The lack of support from cloud-scale buoyancy forces for cloud-scale circulations in the current study indicates that the observed cloud-scale humidity fluxes must be supported by pressure and momentum forces provided by cloud root circulations (cf. Yau 1979). In addition, the large positive values in our extreme buoyancy flux for profile 8, and the observed form of the cloud-scale variances near the surface, are evidence that cloud-scale fluxes are also enhanced by buoyancy and momentum forcing provided by density and raindrop drag–driven downdrafts below precipitating cumuli, which spread into large pools at the surface and displace high-humidity air upwards on cloud scales. It should also be remembered that cloud-scale motion can occur without clouds, and that some of the observed cloud-scale results may be influenced by large boundary layer eddies that have been partitioned into the cloud-scale category.

The small-scale alongwind (x) momentum flux is negative and reduces in magnitude with height (positive slope), arriving at zero at around $z = 1.5h$ (Fig. 6d). The across-wind (y) flux (not shown) is close to zero throughout the SCL and generally has a slightly negative slope, in agreement with the slight counterclockwise turning of the wind immediately above $z = h$ (see sections 2b and 5a). Individual profiles follow these trends with little variation. The cloud-scale fluxes (C_{wu}, C_{wv}) exhibit quite variable behavior in individual profiles, presumably reflecting the interaction of cloud–SCL processes with the variable wind conditions high in the cloud layer. The extreme profiles are likewise scattered.

e. Updrafts and downdrafts in the SCL

The small-scale temperature–humidity correlation (Fig. 7) consistently describes a sweeping asymptotic curve from a positive correlation close to the surface (highest value around 0.6), through zero at $z \simeq 0.1h$ (corresponding to the zero point of the H distributions), and then dropping to a constant value close to -0.9 at cloud base and above. Negative θ–q correlations in the upper SCL have been seen by others (in GATE, Wyngaard and LeMone 1980; in BOMEX, Donelan and Miyake 1973 and McBean 1973), and the height of crossover from positive to negative values reflects the degree of balance between evaporation-driven turbulent transport originating at the surface (positive correlation) and the effects of downward entrainment of warm, dry air from above the SCL (negative correlation).

The cloud-scale correlation term (Fig. 7), although variable in shape, is consistently negative at all levels except close to the surface, where it is close to zero and occasionally slightly positive. In order to obtain the observed cloud-scale latent and sensible heat flux profiles, moist–cool updrafts and dry–warm downdrafts are therefore required through the middle of the SCL. The former may be achieved in the presence of the ambient mean profiles, by cloud root updrafts and forced displacement of air upward in regions above density currents, while the latter comes from downward motion elsewhere. Again, it should be remembered that cloud-scale motions can occur without the presence of clouds, and the negative cloud-scale correlations observed in profiles 1 and 2 may correspond to some large boundary layer eddies that have been partitioned into the cloud-scale category.

The role of cloud-scale updrafts and downdrafts in precipitating conditions is further explored in a brief conditional sampling analysis of the most disturbed profile (rank 8) in Fig. 8. Cloud-scale updrafts are defined as regions (2-km blocks) in which the cloud-scale vertical velocity is greater than half a standard deviation above zero ($\overline{w} > 0.5\sigma_{\overline{w}}$), and downdrafts are defined in the opposite sense ($\overline{w} < -0.5\sigma_{\overline{w}}$). The fraction ($f$) of a

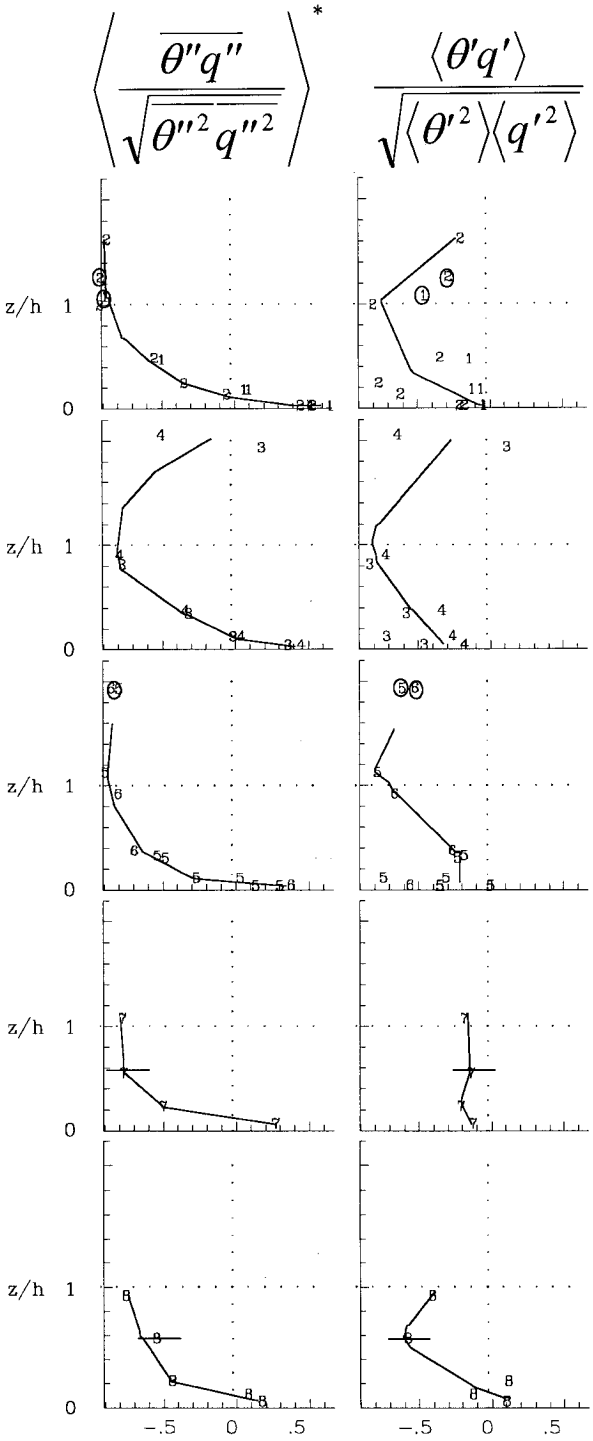

FIG. 7. As for Fig. 6 but temperature–humidity correlations.

run occupied by updrafts is then 0.22 ± 0.05, with a slight minimum at the revised top of the mixed layer ($z = 0.6h$), while that of downdrafts increases from around 0.25 near the surface to 0.41 at $z = h$ (Fig. 8a). Average vertical velocities in updrafts are much larger than in downdrafts (Fig. 8b). Through the bulk of the SCL, cloud-scale updrafts are moist and cool while downdrafts are dry and slightly warm (Figs. 8c and 8d). Near the surface, updrafts can be slightly warm and downdrafts cool. The conclusions of the analysis of θ–q correlations above are thus well confirmed.

Since updrafts are moist and downdrafts are dry, both produce positive cloud-scale latent heat fluxes (see Fig. 8e). Updrafts are much more intense than downdrafts near the (revised) top of the mixed layer but are similar in magnitude near the surface and at $z = h$. Contributions to the overall cloud-scale flux from updrafts and downdrafts are approximately equal when averaged over the depth of the SCL, although updrafts produce a larger contribution near the (revised) mixed layer top and downdrafts dominate near the surface (Fig. 8f). These results are in broad agreement with the CEM study of Krueger (1988), who found that cloud-scale updrafts and downdrafts contribute about equally to warming and drying of the SCL (see his Figs. 11c and 11d).

Small-scale latent heat flux intensities (S_{wq}) within cloud-scale updrafts increase strongly with height through the SCL, in dramatic contrast to those in downdrafts, which decrease with height (Fig. 8g). The latter are, in fact, very nearly zero in the upper mixed layer, with the consequence that updrafts contribute 80% of the total small-scale flux close to cloud-base (Fig. 8h), despite occupying only 28% of the overall area (Fig. 8a). The majority of small-scale vertical humidity transport therefore occurs within cloud root regions in disturbed conditions, indicating that the concept of local enhancement of moisture fluxes in cloudy regions (as discussed in section 5d above) can be extended down to the scale of individual cloud roots (2 km). These results are similar to those of LeMone and Pennell (1976) for momentum flux associated with positive vertical velocities just below trade wind cumulus. The only significant component of the upper-SCL total moisture flux (F_{wq}) outside of cloud root regions is the cloud-scale downdraft component. In Krueger's study, these downdrafts were composed of 1) diluted updraft air (mixed with environmental air) in the wake of strong updrafts and 2) cloud-layer environmental air that flows into the developing downdraft. This process can thus be regarded as being a cloud-scale enhancement of the entrainment process.

In contrast to the disturbed case above, small-scale humidity flux intensities in both updrafts and downdrafts are decreasing with height in the undisturbed profile 1, while in profile 4 (containing strongly developing Cu), they are both increasing (not shown). The latter may indicate that as cloud-scale processes start to become organized, small-scale entrainment from above is initially enhanced, although it is suppressed when the convection becomes more developed. A more detailed conditional sampling analysis, although clearly of interest, is beyond the scope of this study.

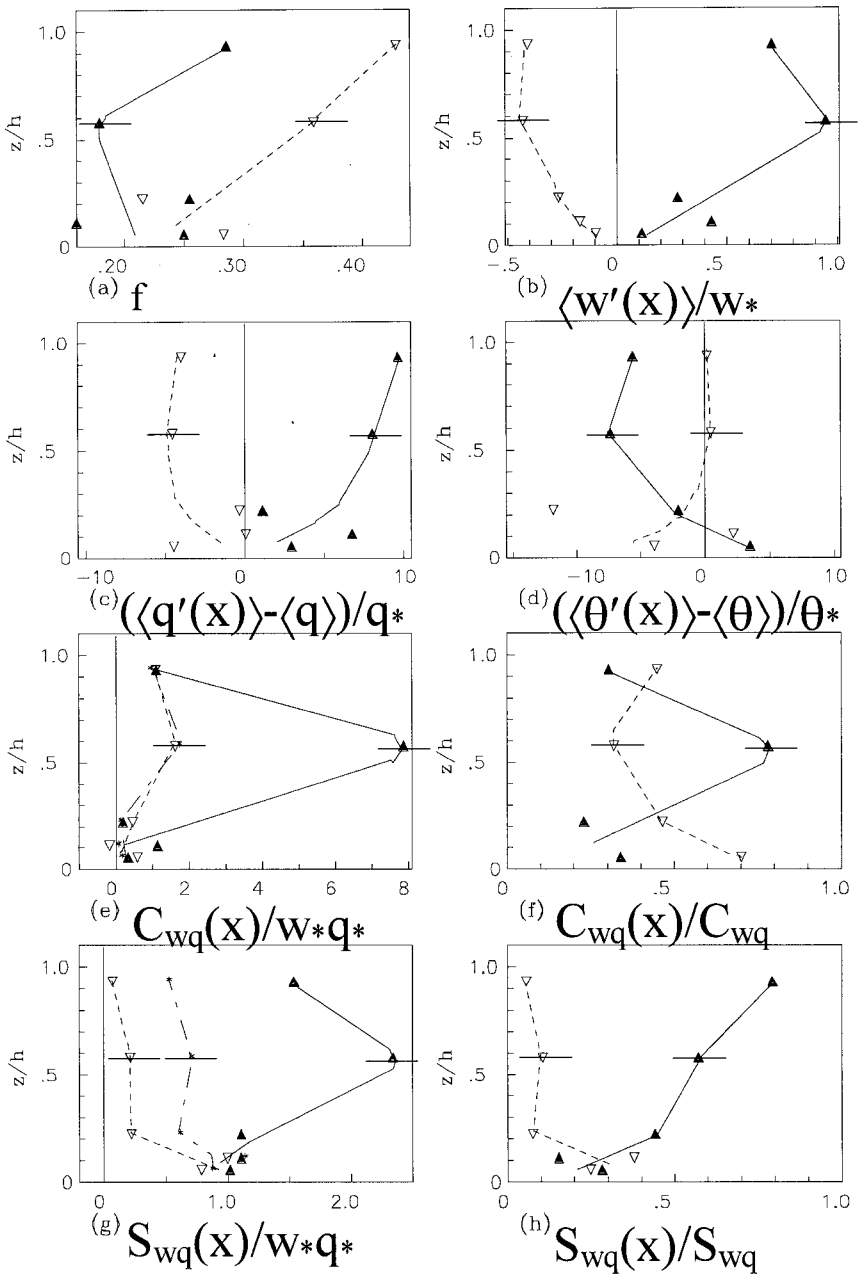

FIG. 8. Vertical distribution of various quantities from the highly disturbed profile 8, partitioned into contributions from strong cloud-scale updrafts (solid up-triangles) and downdrafts (hollow down-triangles). (a) Fraction of entire run occupied by strong updrafts and downdrafts. Intensities of (b) vertical velocity, (c) specific humidity, and (d) potential temperature inside updrafts and downdrafts. (e) Intensity and (f) contribution to the cloud-scale latent heat flux. (g) Intensity and (h) contribution to the small-scale latent heat flux. Asterisks in (e) and (g) represent the combined flux from all categories. See text for details.

6. Summary and discussion

a. Conceptual model of the ABL disturbed by precipitating cumulus

The following brief physical description of the ITCZ SCL under a precipitating cloud cluster is based on the analyses of sections 4 and 5, and is illustrated in Fig. 9.

The ITCZ boundary layer is characterized by vigorous exchange between the cloud and subcloud layers. Variance profiles and temperature–humidity correlations indicate that turbulent entrainment and penetration by cloud-scale downdrafts injects significant amounts of warm–dry air into the SCL from above, leading to sloped profiles of mean quantities. When strongly active

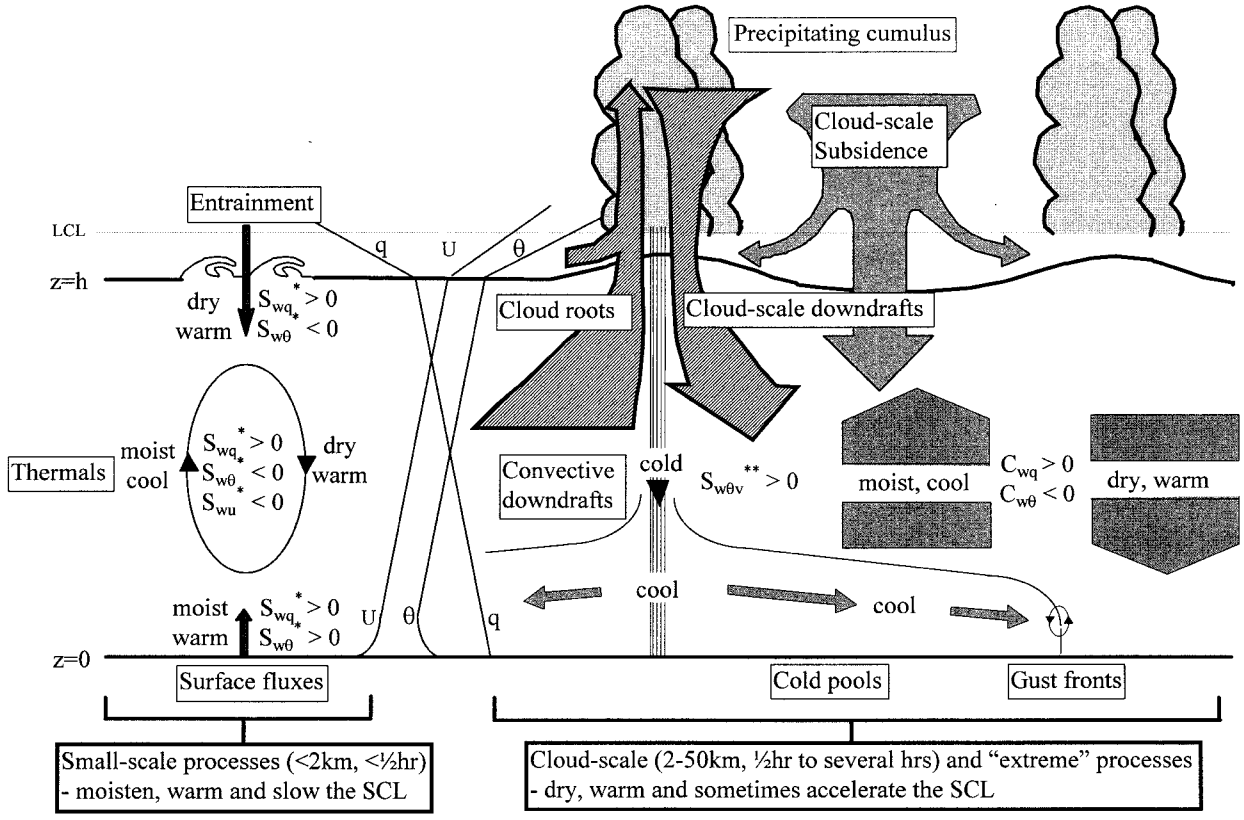

FIG. 9. Schematic representation of transport processes in the ITCZ subcloud layer under a precipitating cloud cluster.

cumulus is present, cloud-scale motions become important. Pressure effects directly below the bases of clouds cause cloud-scale updrafts (cloud roots) to form, and cloud-scale downdrafts containing dry air from the cloud environment invade the SCL. Cloud-scale fluxes are comparable in magnitude to small-scale fluxes at this stage and are contained mainly within the SCL. As cloud and rain processes become well developed, however, cloud-scale processes dominate (humidity variances and fluxes are large at cloud base). Small-scale humidity transport is strongly concentrated into the cloud root areas.

In disturbed conditions, precipitation processes produce pools of evaporatively cooled air below clouds and strong small-scale downdrafts (extreme events) that descend to the surface and spread the cold pools horizontally. These cool fast-moving density currents enhance surface evaporation and heat fluxes, and force convergent motions along the resultant gust fronts (also extreme events). Consequently, the lower SCL becomes strongly heterogeneous, and near-surface variability of temperature and wind components is large. Variances of u and v are symmetrical and do not scale with w_* (see section 6d below). Cold pool outflows also contribute to the direct cloud-scale fluxes in the mid-SCL by displacement of near-surface air upwards.

b. Modification of depth-integrated SCL properties

The bulk impact of increasing clouds and rain upon the TOGA COARE SCL can be neatly summarized with reference to the SCL-integrated convergences of flux components for all profiles (Fig. 10). These were obtained by calculating the gradient of the vertical distribution of the relevant flux between each pair of adjacent flight levels and then forming a weighted average of these gradients for all levels up to $z = h$. The weights used were equal to the difference in scaled height between the two appropriate levels. The summed, or total, flux for quantity a is equivalent to the vertical turbulent-flux tendency term in the SCL-integrated large-scale budget of a [$\Sigma\ (-\partial F_{aw}/\partial z)\Delta(z/h)$]. Unfortunately, a full budget analysis is impossible, since accurate estimates of neither local time changes nor advective terms (both of which are likely to be large in heterogeneous conditions) are obtainable from this dataset.

As the intensity (rank) of cloud activity increases, the rate of modification of SCL-mean quantities by both small- and cloud-scale processes (magnitude of the integrated flux convergences) broadly increases. Small-scale processes lead to overall moistening and warming of the SCL, with the rate of moistening increasing with rank. The only exception is profile 4, in which small-

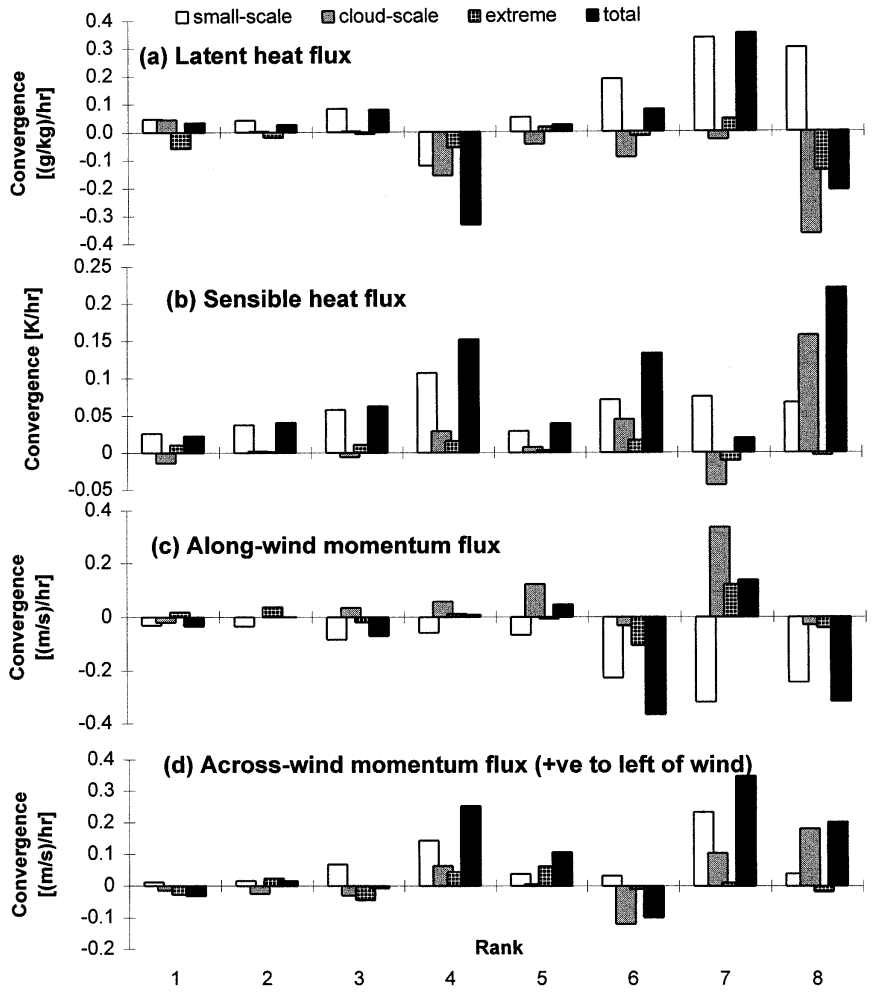

FIG. 10. SCL-integrated convergences of vertical flux components for all profiles. Each overlapping clump of bars indicates (from left to right): small-scale, cloud-scale, extreme, and total flux convergences, integrated over the depth of the SCL. Profiles are presented in order of rank from left to right across the page. See text for details.

scale processes are drying the SCL (E increasing with height). This is presumably related to the strong cloud growth immediately above the flight line during this profile [see section 2a(6)] and may reflect locally enhanced convergence. The small-scale sensible heat flux convergence is also particularly large in profile 4, and the across-wind momentum flux is enhanced (but not the alongwind momentum flux). Modification of the SCL by cloud-scale processes is always minor in the lower ranked profiles, but in profiles 4–8 cloud-scale processes dry and warm the SCL. Thus, small-scale processes mainly inject moisture into the SCL from the surface, while cloud-scale processes remove it from the top (and replace it with drier air from above). The balance between the two (the total flux) leads to overall moistening of the SCL by local processes in all cases except profiles 4 and 8. In profile 8 the reason is that cloud-scale processes have become dominant over small-scale processes, but in profile 4 the reason is that small-scale processes are actually working with cloud-scale processes to dry the SCL. All scales warm the SCL on the whole in these profiles.

The rate of modification of the SCL by momentum fluxes broadly increases with rank. Small-scale alongwind momentum fluxes always slow the SCL air, reflecting the influence of surface friction, while cloud-scale fluxes actually accelerate the SCL flow in four of the eight cases. The latter is dependant upon variations in the wind speed and direction high in the cloud layer. Small-scale across-wind momentum fluxes accelerate the mean SCL flow toward the left of the mean wind in all cases, consistent with the counterclockwise turning of the wind immediately above $z = h$ in these flights. Cloud-scale across-wind momentum fluxes can turn the SCL wind right or left, depending on the variability in wind direction higher in the cloud layer.

It is of interest to compare the results from our most disturbed case (profile 8) with deep convection results

of others. Since the profile 8 latent heat flux extreme term is significant, and contributes in the same sense as the cloud-scale term, we associate this term with cloud processes and add it to the cloud-scale term. Converting both the resultant combined cumulus transport term and the small-scale transport term to temperature units using the psychrometric constant, we arrive at -1.28 and 0.75 K hr^{-1}, respectively. The sum of the two (-0.53 K hr^{-1}) is a little smaller than the vertically integrated total transport term (-0.7 K hr^{-1}) calculated by Brümmer (1979) for GATE disturbed conditions, as expected (since we avoided the largest MCSs). Krueger (1988) found -1.9 K hr^{-1} for this term, made up of -2.4 K hr^{-1} for cumulus transport and 0.5 K hr^{-1} for small-scale transport (see his Table 4). However, he attributed around -1.0 K hr^{-1} of the cumulus transport term to enhanced fluxes associated with random perturbations used to initiate cloud motions in his model.

c. Implications for integral models

The strong relationship observed between wind speed and bulk humidification of the SCL by small-scale processes throughout the profiles is a combined result of both the dependence of surface evaporation upon wind speed (Table 2) and the consistently negative slope (implying moistening) in the small-scale E profiles (the latter can be upset by strong local convergence–advection, as probably occurred in profile 4). In the zero or low precipitation cases under conditions of subsidence, zero or even weak upward vertical motions (profiles 1–5, excluding 4), the observed correlation between windspeed and increased cloud activity (rank; see Table 2) is likely to be caused predominantly by increased transport out of the mixed layer due to increased surface evaporation, with SCL processes remaining dominated by (small scale) surface forcings (entrainment fluxes of buoyancy and humidity being small constant fractions of the surface fluxes). Cloud-scale influences are small, and it is thus likely that useful representations of the depth and mean structure of the convective mixed layer under such conditions could still be provided by one-dimensional zero-order jump or slab models [e.g., review in chapter 6.1, Garratt (1994)]. As cloud motions intensify in response to increasing large-scale vertical motion, however, cloud-scale processes become more significant. Cloud root inflow from the mixed layer and the layer between $z = h$ and cloud base (Fig. 9) is compensated by enhanced cloud-layer subsidence and cloud-scale downdrafts into the mixed layer (see also Sarachik 1974; Johnson 1976, 1977, 1981). As seen above, such fluxes can significantly modify mixed layer properties, including local wind speeds that can then feed back to enhanced surface fluxes (see also Jabouille et al. 1996). These processes represent nonsurface forcings that can significantly change mixed-layer flux profiles and local mean vertical velocities. Continued work is required on adjustments to one-dimensional models: 1) adjustment of subsidence term to account for local cloud-scale subsidence, 2) addition of cloud-scale component to formulation of fluxes at the SCL top to account for cloud updrafts and downdrafts, and 3) enhancement of local near-surface scalar windspeeds to account for momentum entrainment and density-current outflow effects. Given the presence of cloud-scale circulations and density currents, it is also likely that significant local advection terms may affect budgets in these strongly heterogeneous conditions, as seems to be the case in profile 4. Furthermore, as rainfall increases, phase change thermodynamics and SST modifications may become important.

d. Implications for parameterization of surface fluxes

The increase of near-surface horizontal wind variances with rank, as seen in sections 5b and 5c, has important implications for surface flux parameterizations in large-scale models. Bulk methods derived from surface-based measurements, such as that presented by Fairall et al. (1996) for TOGA COARE conditions, do not account for variability on cloud scales as required by large-scale models. Such effects are now starting to be investigated using TOGA COARE datasets (Sun et al. 1996; Jabouille et al. 1996), including a forthcoming study by the present authors. As a first step, it is useful to investigate the dependence of the surface value of the all-scale horizontal turbulent kinetic energy, $\mathrm{TKE_H} = 0.5(S_{uu} + C_{uu} + S_{vv} + C_{vv})$, upon large-scale vertical motion. An estimate of the mean vertical velocity near cloud base is given, via the continuity equation, by $w_h = -h$*Div, where Div is the 1000-hPa large-scale horizontal divergence (given in Table 2), which is assumed to be constant from the surface to $z = h$. The surface $\mathrm{TKE_H}$ is plotted versus w_h in Fig. 11a, where it is seen that a strong dependence begins soon after w_h turns positive. In analogy to the introduction of a gustiness velocity to compensate for the effects of intrusion by mixed layer eddies into the surface layer under convective conditions on scales up to the mixed-layer height (Godfrey and Beljaars 1991), we formulate a deep convective velocity scale applicable at the surface:

$$w_{\mathrm{con}} = w_* + \alpha w_H, \qquad \alpha = \begin{cases} 0, & w_H \le 0 \\ c, & w_H > 0, \end{cases}$$

where the nondimensional constant c is chosen so as to optimize a least squares linear fit between $\mathrm{TKE_H}(0)$ and w_{con}^2, constrained to pass through the origin. A value of $c = 220$ is obtained, achieving a least squares coefficient of determination of 0.975 (Fig. 11b). As expected, when $\mathrm{TKE_H}$ is then normalized with w_{con}^2 rather than w_*^2, the results show a substantially reduced dependance upon rank (Figs. 11c and 11d).

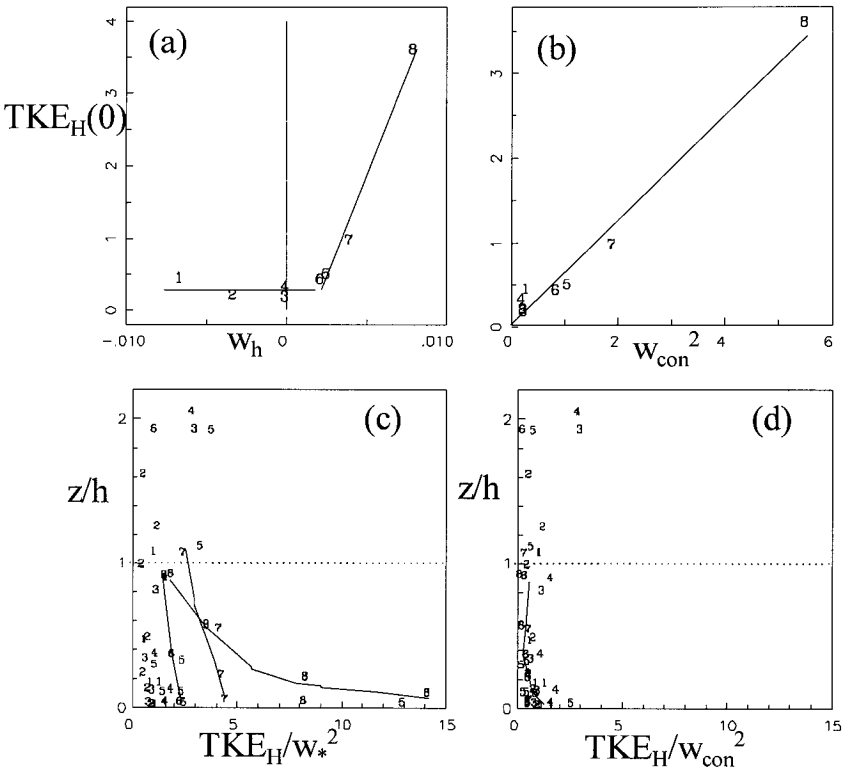

FIG. 11. (a) Total (all scale) horizontal turbulent kinetic energy (TKE_H) near the surface, as a function of large-scale mean vertical velocity at cloud base (w_h); (b) surface TKE_H as a function of the square of the deep convective velocity scale, w_{con} (slope of least squares regression line through origin: 0.63826; $r^2 = 0.975$); (c) vertical distribution of TKE_H, normalized using w_*; and (d) vertical distribution of TKE_H, normalized using w_{con}. See text for details.

7. Conclusions

This study has analyzed the structure of the ITCZ SCL during various stages of a developing precipitating cloud cluster. The range of conditions encountered fill the gap between those of the GATE fairweather ABL investigated by Nicholls and LeMone (1980) and the developed stage of major convective disturbances studied by Brümmer (1979), Barnes and Garstang (1982), and others. Many aspects of SCL structure inferred indirectly from budget, diagnostic, and observational studies have been conclusively verified by our in situ aircraft results. Such studies cannot make the important separation between small- and cloud-scale processes, however. For the ITCZ SCL, such a separation has only been achieved previously in the CEM study of Krueger (1988), the results of which have now also been verified by ours. Previously unseen for this ABL have been the form of the variances, momentum fluxes, and θ–q correlations, split into small- and cloud-scale components. Along with the conditional sampling analysis, these results have highlighted the role of cloud-scale circulations and density currents in the modification of SCL properties. Of particular interest has been the apparent enhancement of small-scale updrafts in the cloud root regions (presumably due to increased surface wind speeds associated with cloud-root circulations) and the identification of w_h as a potentially useful surface scaling parameter.

The partitioning of results into contributions from small-scale, cloud-scale, and extreme processes has proven to be a useful technique. Extreme events (downdrafts, gust fronts, and the possible effects of moisture contamination) are closely related to cloud processes, and their role in ABL transport becomes more important in disturbed conditions. Their main effect is to skew the distribution of small-scale fluxes, and removal using the mean–mode technique has led to significant reduction in the scatter of small-scale distributions. This, and the generally good comparison of small-scale variance and flux distributions with those from other nonprecipitating ABLs, despite the presence of often large cloud-scale terms (especially variances), is strong evidence that the two scales of motion are separable. This is a useful result in the light of our evidence that small-scale processes in the ITCZ SCL may still be representable by existing theories on ABL structure (perhaps with slight modifications to accomodate the effects of enhanced horizontal velocity variances by cloud-scale processes). In disturbed conditions, cloud-scale (20–50 km) processes are clearly also important, however, and should be rep-

resented in the subgrid parameterizations of climate and weather models.

Acknowledgments. The majority of this work has been supported by grants and a fellowship provided by the Australian Research Council. The first author recognizes the additional support of an Alexander von Humboldt Foundation Fellowship in 1994, during which time some of the data analysis work was begun. Large-scale 1000-hPa ECMWF divergence analysis charts for the TOGA COARE area were provided courtesy of J. L. Redelsperger (Meteo France).

REFERENCES

Asencio, N., J. P. Lafore, P. Pires, and J. L. Redelsperger, 1993: Analyses quotidiennes du CEPMMT durant la periode d'observations intensives de l'experience TOGA/COARE. *CNRM/GMME Note de Travail*, 12, 243 pp. [Available from Meteo France CNRM/GMME, 42 Avenue Gustave Coriolis, 31057 Toulouse Cedex, France.]

Augstein, E., H. Riehl, F. Ostapoff, and V. Wagner, 1973: Mass and energy transports in an undisturbed Atlantic trade-wind flow. *Mon. Wea. Rev.,* **101,** 101–111.

Barnes, G. M., and M. Garstang, 1982: Subcloud layer energetics of precipitating convection. *Mon. Wea. Rev.,* **110,** 102–117.

Brümmer, B., 1979: Boundary layer processes during the life cycle of GATE convective disturbances. *Beitr. Phys. Atmos.,* **52,** 306–330.

Charba, J., 1974: Application of gravity current model to analysis of squall-line gust front. *Mon. Wea. Rev.,* **102,** 140–156.

Chou, S. H., D. Atlas, and E. N. Yeh, 1986: Turbulence in a convective marine atmospheric boundary layer. *J. Atmos. Sci.,* **43,** 547–564.

Donelan, M., and M. Miyake, 1973: Spectra and fluxes in the boundary layer of the trade wind zone. *J. Atmos. Sci.,* **30,** 444–464.

Echternacht, K. L., and M. Garstang, 1976: Changes in the structure of the tropical subcloud layer from the undisturbed to disturbed states. *Mon. Wea. Rev.*, **104,** 407–417.

Emanuel, K. A., 1987: An air–sea interaction model of intraseasonal oscillations in the tropics. *J. Atmos. Sci.,* **44,** 2324–2340.

Emmitt, G. D., 1978: Tropical cumulus interaction with and modification of the subcloud region. *J. Atmos. Sci.,* **35,** 1485–1502.

Esbensen, S., 1975: An analysis of subcloud-layer heat and moisture budgets in the western Atlantic trades. *J. Atmos. Sci.,* **32,** 1921–1933.

Fairall, C. W., 1984: Wind shear enhancement of entrainment and refractive index structure parameter at the top of a turbulent mixed layer. *J. Atmos. Sci.,* **41,** 3472–3484.

——, E. F. Bradley, D. P. Rogers, J. B. Edson, and G. S. Young, 1996: Bulk parameterization of air-sea fluxes for TOGA COARE. *J. Geophys. Res.*, **101,** 3747–3764.

Garratt, J. R., 1994: *The Atmospheric Boundary Layer*. Cambridge University Press, 316 pp.

Godfrey, J. S., and A. C. M. Beljaars, 1991: On the turbulent fluxes of buoyancy, heat and moisture at the air-sea interface at low wind speeds. *J. Geophys. Res.,* **96,** 22 043–22 048.

Goff, R. C., 1976: Vertical structure of thunderstorm outflows. *Mon. Wea. Rev.,* **104,** 1429–1440.

Gregory, D., and M. J. Miller, 1989: A numerical study of the parameterization of deep tropical convection. *Quart. J. Roy. Meteor. Soc.,* **115,** 1209–1241.

Gultepe, I., A. J. Heymsfield, and D. H. Lenschow, 1990: A comparison of vertical velocity in cirrus obtained from aircraft and lidar divergence measurements during FIRE. *J. Atmos. Oceanic Technol.,* **7,** 58–67.

Houze, R. A., Jr., and C. P. Cheng, 1977: Radar characteristics of tropical convection observed during GATE: Mean properties and trends over the summer season. *Mon. Wea. Rev.,* **105,** 964–980.

Jabouille, P., J. L. Redelsperger, and J. P. LaFore, 1996: Modification of surface fluxes by atmospheric convection in the TOGA COARE region. *Mon. Wea. Rev.,* **124,** 816–837.

Johnson, R. H., 1976: The role of convective-scale precipitation downdrafts in cumulus- and synoptic-scale interaction. *J. Atmos. Sci.,* **33,** 1890–1910.

——, 1977: Effects of cumulus convection on the structure and growth of the mixed layer over south Florida. *Mon. Wea. Rev.,* **105,** 713–724.

——, 1981: Large-scale effects of deep convection on the GATE tropical boundary layer. *J. Atmos. Sci.,* **38,** 2399–2413.

Khalsa, S. J. S., and G. K. Greenhut, 1987: Convective elements in the marine atmospheric boundary layer. Part II: Entrainment at the capping inversion. *J. Climate Appl. Meteor.,* **26,** 824–836.

Krueger, S. K., 1985: Numerical simulation of tropical cumulus clouds and their interaction with the subcloud layer. Ph.D. dissertation, University of California, 205 pp.

——, 1988: Numerical simulation of tropical cumulus clouds and their interaction with the subcloud layer. *J. Atmos. Sci.,* **45,** 2221–2250.

LeMone, M. A., 1980a: On the difficulty of measuring temperature and humidity in cloud: Comments on ''Shallow convection on Day 261 of GATE: Mesoscale arcs.'' *Mon. Wea. Rev.,* **108,** 1702–1705.

——, 1980b: The marine boundary layer. Preprints, *Proc. Workshop on the Planetary Boundary Layer*, Boulder, CO, Amer. Meteor. Soc., 182–246.

——, and W. T. Pennell, 1976: The relationship of trade wind cumulus distribution to subcloud layer fluxes and structure. *Mon. Wea. Rev.,* **104,** 525–539.

——, and R. J. Meitin, 1984: Three examples of fairweather boundary-layer convection in the tropics. *Mon. Wea. Rev.,* **112,** 1985–1997.

——, G. M. Barnes, J. C. Fankhauser, and L. F. Tarleton, 1987: Perturbation pressure fields measured by aircraft around the cloud-case updraft of deep convective clouds. *Mon. Wea. Rev.,* **115,** 312–326.

——, L. F. Tarleton, and G. M. Barnes, 1988: Perturbation pressure at the base of cumulus clouds in low shear. *Mon. Wea. Rev.,* **116,** 2063–2068.

Lenschow, D. H., and W. T. Pennell, 1974: On the measurement of in-cloud and wet-bulb temperatures from an aircraft. *Mon. Wea. Rev.,* **102,** 447–454.

Lin, X., and R. H. Johnson, 1996: Kinematic and thermodynamic characteristics of the flow over the western Pacific warm pool during TOGA COARE. *J. Atmos. Sci.,* **53,** 695–715.

Lipps, F. B., and R. S. Hemler, 1986: Numerical simulation of deep tropical convection associated with large-scale convergence. *J. Atmos. Sci.,* **43,** 1796–1816.

Lopez, R. E., 1973: Cumulus convection and larger scale circulations II. Cumulus and mesoscale interactions. *Mon. Wea. Rev.,* **101,** 856–870.

——, 1976: Radar characteristics of the cloud populations of tropical disturbances in the northwest Atlantic. *Mon. Wea. Rev.,* **104,** 268–283.

——, 1977: The lognormal distribution and cumulus cloud populations. *Mon. Wea. Rev.,* **105,** 865–872.

Mandics, P. A., and F. F. Hall, 1976: Preliminary results from the GATE acoustic echo sounder. *Bull. Amer. Meteor. Soc.,* **57,** 1142–1147.

McBean, G. A., 1973: Comparison of the turbulent transfer processes near the surface. *Bound.-Layer Meteor.,* **4,** 265–274.

Neelin, J. D., I. M. Held, and K. H. Cook, 1987: Evaporation-wind feedback and low-frequency variability in the tropical atmosphere. *J. Atmos. Sci.,* **44,** 2341–2348.

Nicholls, S., and M. A. LeMone, 1980: The fair weather boundary layer in GATE: The relationship of subcloud fluxes and structure

to the distribution and enhancement of cumulus clouds. *J. Atmos. Sci.,* **37,** 2051–2067.

——, ——, and G. Sommeria, 1982: The simulation of a fairweather marine boundary layer in GATE using a three-dimensional model. *Quart. J. Roy. Meteor. Soc.*, **108,** 167–190.

Ötles, Z., and J. A. Young, 1996: Influence of shallow cumuli on subcloud turbulence fluxes analyzed from aircraft data. *J. Atmos. Sci.,* **53,** 665–676.

Pennell, W. T., and M. A. LeMone, 1974: An experimental study of turbulence structure in the fair-weather trade wind boundary layer. *J. Atmos. Sci.*, **31,** 1308–1323.

Riehl, H., C. Yeh, J. S. Malkus, and N. E. La Seur, 1951: The northeast trade of the Pacific Ocean. *Quart. J. Roy. Meteor. Soc.*, **77,** 598–626.

Rotunno, R., and J. B. Klemp, 1982: The influence of the shear-induced pressure gradient on thunderstorm motion. *Mon. Wea. Rev.*, **110,** 136–151.

Sarachik, E. S., 1974: The tropical mixed layer and cumulus parameterization. *J. Atmos. Sci.,* **31,** 2225–2230.

Simpson, J., and G. van Helvoirt, 1980: GATE cloud-subcloud layer interactions examined using a three-dimensional cumulus model. *Beitr. Phys. Atmos.,* **53,** 106–134.

Soong, S.-T., and W.-K. Tao, 1980: Response of deep tropical cumulus clouds to mesoscale processes. *J. Atmos. Sci.,* **37,** 2016–2034.

Stull, R. B., 1985: A fair-weather cumulus cloud classification scheme for mixed-layer studies. *J. Climate Appl. Meteor.*, **24,** 49–56.

Sun, J., L. Mahrt, S. K. Esbensen, J. F. Howell, C. M. Greb, R. Grossman, and M. A. LeMone, 1996: Scale dependence of air-sea fluxes over the western equatorial Pacific. *J. Atmos. Sci.*, **53,** 2997–3012.

Thompson, R. M., Jr., S. W. Payne, E. E. Recker, and R. J. Reed, 1979: Structure and properties of synoptic-scale wave disturbances in the Intertropical Convergence Zone of the eastern Atlantic. *J. Atmos. Sci.*, **36,** 53–72.

Webster, P. J., and R. Lukas, 1992: TOGA COARE: The coupled ocean–atmosphere response experiment. *Bull. Amer. Meteor. Soc.,* **73,** 1377–1416.

Williams, A. G., H. Kraus, and J. M. Hacker, 1996: Transport processes in the tropical warm pool boundary layer. Part I: Spectral composition of fluxes. *J. Atmos. Sci.,* **53,** 1187–1202.

Wyngaard, J. C., and M. A. LeMone, 1980: Behavior of the refractive index structure parameter in the entraining convective boundary layer. *J. Atmos. Sci.,* **37,** 1573–1585.

Xu, K.-M., and S. K. Krueger, 1991: Evaluation of cloudiness parameterizations using a cumulus ensemble model. *Mon. Wea. Rev.,* **119,** 342–367.

——, A. Arakawa, and S. K. Krueger, 1992: The macroscopic behavior of cumulus ensembles simulated by a cumulus ensemble model. *J. Atmos. Sci.,* **49,** 2402–2420.

Yau, M. K., 1979: Perturbation pressure and cumulus convection. *J. Atmos. Sci.*, **36,** 690–694.

Young, G. S., 1988: Turbulence structure in the convective boundary layer. Part I: Variability of normalized turbulence statistics. *J. Atmos. Sci.*, **45,** 719–726.

Zipser, E. J., 1977: Mesoscale and convective-scale downdrafts as distinct components of squall-line structure. *Mon. Wea. Rev.*, **105,** 1568–1589.